ACCSCIENCE PUBLISHING

International Journal of Bioprinting

RESEARCH ARTICLE

# Fibrous bioinks for bioprinting anisotropic micro- and nanoscale scaffolds: A novel strategy for *in vitro* skeletal muscle engineering

**Gerardina Ruocco[1,2,3†], Elena Marcello[1,2,3†*], Camilla Paoletti[1,2,3], Massimo Salvi[2,4], Alice Zoso[1,2,3], Mattia Spedicati[1,2,3], Irene Carmagnola[1,2,3‡], and Valeria Chiono[1,2,3‡]**

[1]Department of Mechanical and Aerospace Engineering, Politecnico di Torino, Turin, Italy

[2]PolitoBIOMed Lab, Politecnico di Torino, Turin, Italy

[3]Interuniversity Center for the Promotion of 3Rs Principles in Teaching and Research, Pisa, Italy

[4]Department of Electronics and Telecommunications, Politecnico di Torino, Turin, Italy

(This article belongs to the *Special Issue*: *Biofabrication Breakthroughs: Innovation and Application in Bioprinting, Biomaterials, and Organoid*)

## Abstract

Replicating skeletal muscle architecture remains challenging in 3D bioprinting, as conventional bioinks lack multiscale directional cues. Herein, we propose a next-generation fibrous bioink composed of fragmented electrospun gelatin fibers (f-GFs), uniformly embedded in an alginate/gelatin hydrogel matrix (f-ALG/Gel). Upon microextrusion bioprinting, shear-induced f-GF alignment enabled the fabrication of microfilament-based scaffolds with intrinsic anisotropy. The resulting constructs exhibited high shape fidelity, favorable viscoelastic properties, and physiologically relevant stiffness (Young's modulus: 16.1 ± 1.7 kPa). *In vitro* studies using C2C12 murine myoblasts demonstrated that the embedded f-GFs provided strong topographical guidance, enhancing cell alignment and myogenesis. After 14 days of culture, the f-ALG/Gel scaffolds supported a 2.5-fold increase in myotube fusion index and length, alongside reduced angular dispersion. These effects were achieved without the need for biochemical induction with a differentiation medium, underscoring the key role of structural cues at the micro- and nanoscale in C2C12 differentiation and maturation. In conclusion, this work proposes a scalable, cell-compatible strategy to recapitulate the hierarchical organization of skeletal muscle tissue within 3D-printed constructs. The platform holds broad potential for applications in regenerative medicine, skeletal muscle tissue modeling, and the engineering of cultured meat.

***Keywords:*** anisotropy; 3D bioprinting; fibrous bioinks; skeletal muscle; topographical cue

†These authors contributed equally to this work

‡These authors contributed equally as senior authors

***Corresponding author:**
Gerardina Ruocco
(gerardina.ruocco@polito.it)

**Citation:** Ruocco G, Marcello E, Paoletti C, *et al*. Fibrous bioinks for bioprinting anisotropic micro- and nanoscale scaffolds: A novel strategy for *in vitro* skeletal muscle engineering.
*Int J Bioprint*. 2026;12(1):323-347.
doi: 10.36922/IJB025440455

**Received:** July 2, 2025
**Revised:** October 30, 2025
**Accepted:** November 10, 2025
**Published Online:** November 10, 2025



## 1. Introduction

Skeletal muscle tissue (SMT) accounts for 40–45% of body mass and is essential for movement, metabolism, and homeostasis.[1,2] While minor damage can be repaired by resident stem cells,[3,4] volumetric muscle loss (VML) exceeds this capacity.[5] Traditional

reconstructive surgery, based on autologous tissue transfer (free tissue flaps) and bracing, is limited by insufficient tissue regeneration and functional recovery owing to implant mismatch and donor site morbidity.[6–9] SMT engineering strategies hold promise to restore muscle function and architecture to pre-injury levels, offering therapeutic potential for VML and muscle diseases, such as muscular dystrophies.

Beyond therapeutic applications, engineered SMT is increasingly pursued for disease modeling and preclinical drug testing to better understand muscle-related diseases and/or to explore new therapeutic solutions, overcoming the limitations of traditional drug discovery-to-clinic pipelines.[10] More recently, SMT engineering is gaining attention for cultured meat production, offering an ethical alternative to animal-derived meat, while tackling concerns related to environmental impact and public health.[6,7] Key to SMT engineering is the design of biomimetic scaffolds, mimicking the native-like extracellular matrix (ECM) of SMT, thereby regulating biological functions, facilitating cell–cell communication, and providing the mechanical, topographical, and biochemical cues essential for myoblast alignment, fusion, and myogenesis.[11]

*In vivo*, SMT is a highly organized and hierarchical tissue predominantly consisting of long multinucleated muscle fibers (i.e., myofibers) filled with contractile proteins organized into sarcomeres. Guided by the anisotropic biophysical microenvironment (e.g., ECM architecture and elasticity), myoblasts undergo differentiation and fusion, forming bundles of parallelly aligned myofibers able to contract unidirectionally.[12] To promote cell orientation and myogenic development *in vitro*, engineered anisotropic scaffolds, replicating the SMT structure, are highly sought.

Several tissue engineering methods have been proposed to induce *in vitro* cell alignment through grooved or ridged micro/nanopatterned substrates,[13] nanofibers,[14] hydrogels,[5] chemical surface patterning,[13] mechanical stimulation,[15] and exposure to electrical or magnetic fields.[16] Among them, electrospinning has emerged as a simple and versatile technique for the preparation of aligned nanofibrous structures from a wide variety of biomaterials, with the potential to operate under mild processing conditions.[11] Although electrospun fibers effectively provide directional cues for cell anisotropy and myogenesis, they are unable to replicate the 3D SMT structure.

On the other hand, 3D microextrusion bioprinting enables precise deposition of cells and biomaterials, resulting in 3D constructs with biomimetic composition and mechanical properties. Strand-like bioprinted microstructures may reproduce the architectural bundle-like structure of SMTs. Indeed, bioprinting shear stresses may unfold and orient bioink polymeric chains and align embedded fillers and/or cells, producing hierarchical anisotropic constructs.[8,9,17,18]

Recently, innovative fibrous bioinks, based on hydrogels with embedded micro- and nanofibers, have been proposed for the engineering of *in vivo*-like anisotropic tissues, such as cardiac tissue and tendon.[19] Fibrous bioinks may overcome the lack of 3D topographical cues of conventional hydrogel bioinks and have demonstrated tunable mechanical stiffness, viscoelastic properties, stability, and printability. Prendergast *et al.*[19] developed anisotropic gelatin (Gel) methacryloyl (GelMA)-based hydrogels by bioprinting constructs with embedded norbornene-modified hyaluronic acid microfibers. Although the method supported cell alignment and viability across multiple cell types, the fiber fragmentation process was poorly scalable, as it involves manual extrusion through syringes and filtration. Additionally, the fibrous bioink with the maximum GelMA concentration (5%), which allows for preserving cell viability, showed a limited stiffness (< 3 kPa), which is suboptimal for the engineering of cardiac tissue[20] and SMT.[21] Meanwhile, Choi *et al.*[22] developed a microfiber-infused ink by embedding fragmented fibronectin-coated Gel fibers (GFs) into pre-crosslinked alginate/Gel (ALG/Gel) hydrogels for cardiac tissue engineering. Although postprinted scaffolds supported the formation of anisotropic, functional cardiac tissue, the need for pre-crosslinking required high extrusion pressures, making the approach unsuitable for cytocompatible bioprinting.

To the best of our knowledge, only a few studies have investigated the use of fibrous bioinks for SMT applications. Kamaraj *et al.*[23] proposed a silk microfiber-reinforced silk fibroin hydrogel for *in situ* 3D handheld bioprinting for VML treatment. Although the engineered scaffolds provided structural support and fiber alignment, silk fibroin fibers were fragmented via NaOH-based hydrolysis, a method that may leave cytotoxic residues, reduce molecular weight, and mechanical integrity, and is poorly suited for large-scale production due to environmental impact and morphological variability. Li *et al.*[24] developed a fibrin/GelMA bioink that supports myotube formation through the combined effect of the hydrogel's viscoelastic properties and the fibrillar structure of fibrin. Although these scaffolds showed potential for repairing VML *in vivo*, the approach is restricted to fibril-forming biomaterials (e.g., fibrin or collagen) and does not employ electrospinning.

Currently, fibrous bioinks have not been optimized for SMT bioprinting, despite their potential to impart biophysical directional cues at the nano- and microscales that are crucial for SMT maturation. In this study, we

addressed this gap by developing a novel 3D-bioprinted fibrous scaffold specifically designed to replicate the hierarchical anisotropy of native SMT. A novel fibrous bioink was designed with the ability to acquire an oriented micro-/nanostructure upon microextrusion printing of fibrous hydrogel precursors under mild processing conditions. The bioink was able to undergo rapid crosslinking postprinting under cytocompatible conditions to stabilize scaffold anisotropy, preventing swelling and spreading at the nozzle exit.[25] Electrospun GFs were mechanically fragmented (f-GFs) for the first time in SMT engineering. Unlike chemical dissolution, mechanical fragmentation provides a simple, solvent-free, and highly scalable method to generate short, cell-adhesive fiber fragments. This process preserves native fiber diameter and surface morphology, allows precise control over fragment length, and achieves sufficient yields for bioink formulation. Incorporated into a hydrogel, f-GFs can be aligned through extrusion shear, imparting multiscale anisotropy that closely mimics the hierarchical organization of SMT. By introducing this strategy, our work establishes a new design principle for fiber-reinforced bioinks, advancing beyond classical electrospinning or chemical modification approaches.

Specifically, f-GFs were homogeneously dispersed onto the ALG/Gel prehydrogel matrix (f-ALG/Gel), and, during microextrusion bioprinting, provided anisotropic architectural cues. The printed structures were rapidly stabilized by dual crosslinking with calcium ions and microbial transglutaminase (mTG), yielding constructs with mechanical properties comparable to native muscle tissue. Parallel microfilaments embedded with oriented f-GFs and C2C12 cells replicated the hierarchical anisotropy of SMT, with cells forming aligned, multinucleated myofibers within 14 days of culture. Myotube maturation (area, length, alignment, and fusion index) was quantitatively assessed using a fully automated image analysis pipeline, confirming that bioprinted f-ALG/Gel constructs promote the formation of mature myofibers with biomimetic organization. This strategy paves the way for next-generation SMT therapies and *in vitro* models, replacing C2C12 cells with human primary or human-induced pluripotent stem cell (hiPSC)-derived myoblasts. Beyond healthcare, these fibrous bioinks could also be harnessed to bioprint cultured meat by embedding primary animal myoblasts.

## 2. Materials and methods

### 2.1. Materials

Gelatin (300 g bloom, Type A, porcine skin, suitable for cell culture), phosphate-buffered saline (PBS) tablets, 3-glycidyloxypropyl trimethoxysilane (GPTMS, ≥ 98%), bovine serum albumin (BSA), and Hank's balanced salt solution (HBSS) were obtained from Sigma-Aldrich (United States [US]). mTG from *Streptoverticillium mobaraense* (ACTIVA WM, 85–135 U/g) was supplied by Ajinomoto Co., Inc. (Japan). Sodium alginate (ALG, alginic acid sodium salt, medium viscosity) was purchased from MP Biomedicals (US). Glacial acetic acid (AA, $C_2H_4O_2$, molecular weight: 60.05 g/mol), 10% fetal bovine serum (FBS), 1% penicillin/streptomycin, 2% *L*-glutamine, and Dulbecco's modified Eagle medium (DMEM) were acquired from Thermo Fisher Scientific (US), while absolute anhydrous ethanol was obtained from Carlo Erba (Italy). Calcium chloride ($CaCl_2$, ≥ 95%) was obtained from Fluka Analytical (Switzerland).

### 2.2. Gelatin fiber fabrication and fragmentation

The Gel was electrospun using the NovaSpider instrument (NovaSpider v5, Nadatech Innovations, US). Gel powder was dissolved in a mixture of AA and ultrapure water (AA:water, 75:25 v/v) under constant magnetic stirring to obtain a 20% w/v homogeneous solution. GFs were covalently stabilized using GPTMS, a silane coupling agent selected based on preliminary optimization and literature reports to ensure effective crosslinking while preserving cytocompatibility.[26,27] To enable Gel crosslinking, GPTMS (1.84% v/v) was added and stirred for 40 min at room temperature (RT; 25°C).[28] Then, the Gel–GPTMS solution was loaded into a 5 mL syringe, coupled to a Teflon capillary, and connected to a metal needle (21G) and driven by a high-voltage power supply. Aligned nanofibers (A-Gels) were produced onto an aluminum-covered rotating mandrel (250 mm length × 70 mm diameter; (NovaSpider v5, Nadatech Innovations, US), using the following process parameters: 4,000 rpm mandrel rotation, 28 kV voltage, 1,500 µL/h flow rate, 10 cm needle-collector distance at RT. The electrospun mats were placed under a chemical hood for 48 h to allow complete solvent evaporation and crosslinking. The f-GFs were then obtained via mechanical fragmentation of A-Gel membranes, according to a previously reported protocol.[29] In detail, A-Gel mats were cut into 1 × 1 cm specimens, weighed, and immersed in cold ethanol to a final concentration of 1 mg/mL. A-Gel mats were fragmented using a PT 1200E homogenizer (Polytron, Indonesia) for 10 cycles of 30 s at 25,000 rpm, with the solution kept ice-cooled throughout. The obtained f-GFs were centrifuged at 8,000 rpm for 8 min to remove ethanol. The resulting pellets were collected, and any residual ethanol was evaporated under a laminar-flow hood. Subsequently, the pellets were promptly resuspended in sterile PBS or DMEM for further use.

### 2.3. Gelatin fiber characterization

A-Gel surface morphology was examined by scanning electron microscopy (SEM; TESCAN VEGA SEM platform, TESCAN Orsay Holdings, Czech Republic). Before the analysis, scaffold specimens were sputter-coated with gold using the AGB7234 high-resolution sputter coater (Agar Scientific Ltd, UK). The acquired images were processed through ImageJ/FIJI software (National Institutes of Health, US), and the average fiber diameter was calculated ($n \geq 50$, from three different images). The ImageJ/FIJI directionality tool (Fourier-transform-based analysis) was exploited to measure the fiber anisotropy degree. A-Gel surface wettability was evaluated by static water contact angle (WCA) measurements with the Krüss Drop Shape Analyzer-DSA25 device (Krüss GmbH, Germany). WCA analysis was performed by selecting the Sessile Drop tool, and data were processed using Krüss Drop Shape Analysis software (Krüss GmbH, Germany). Specifically, three drops of deionized water (2 µL) were carefully deposited on the surface of each sample ($n = 3$), and 100 frames per second were acquired using the high-frame-rate camera. Tangent fitting for the drop shape was implemented to calculate both right and left angles.

To investigate fiber chemistry after fragmentation, attenuated total reflectance (ATR)-FTIR spectroscopy was performed. Specifically, 100 µL of f-GF suspension (5 mg/mL in PBS) was dried for 48 h. Spectra were recorded on a Thermo Scientific Nicolet iS50 FTIR Spectrometer (US) equipped with a diamond crystal ATR accessory, with a wavelength range of 4,000–600 $cm^{-1}$ and a resolution of 4 $cm^{-1}$ using 32 scans per sample. A Gel powder was used as the control. f-GF morphology and length distribution were evaluated through brightfield microscopy (A1 HD25, Nikon, Japan). A suspension of f-GFs was pipetted onto a microscope slide for imaging: 40 images were captured, and 150 single f-GFs were analyzed using the Line tool provided by the ImageJ/FIJI program.

### 2.4. Hydrogel formulation and optimization

A stock ALG solution (8% w/v, 5 mL) was prepared by dissolving ALG powder in PBS under mild magnetic stirring overnight at RT. The solution was then transferred into a 5 mL syringe and centrifuged at 4,000 rpm for 5 min to remove air. Similarly, an 8% w/v Gel stock solution (5 mL) was prepared by dissolving Gel powder in PBS with magnetic stirring overnight at 50°C. The stock solutions were subsequently combined using an appropriate volume of PBS diluent to produce homogeneous ALG/Gel solutions at final polymer concentrations of 6, 8, and 10% w/v (ALG:Gel, 30:70% w/w). ALG/Gel or f-ALG/Gel hydrogel precursors were cast and incubated for 10 min at RT before undergoing dual crosslinking via ionic and enzymatic mechanisms. Crosslinking solutions containing 0.1 M $CaCl_2$ and different concentrations of mTG (2.5%, 5%, and 10% w/v) were prepared following an optimized protocol,[18] vortexed until fully dissolved, and stored in the dark. All solutions were sterilized using 0.22 µm filters. Each sample (120 µL) was immersed in 500 µL of the mTG+$Ca^{2+}$ solution for 15 min at RT, after which the crosslinked scaffolds were rinsed twice with HBSS to remove any unreacted residues.

For biological experiments, ALG powder was washed three times in absolute ethanol for 10 min and exposed to UV light for 1 h prior to solubilization. The Gel stock solution was sterilized by filtering through 0.22 µm filters. To formulate fibrous hydrogels (f-ALG/Gel), f-GFs were diluted in PBS and subsequently mixed with ALG and Gel stock solutions, as described above, to achieve final fiber concentrations of 1% and 2% w/v (f-ALG/Gel [1%] and f-ALG/Gel [2%]). F-ALG/Gel hydrogels were dual-crosslinked as described above.

### 2.5. Fibrous hydrogel characterization

#### *2.5.1. Rheology*

Rheological experiments were carried out using an MCR 302 rheometer (Anton Paar, Austria), equipped with a parallel plate geometry (25 mm diameter and 0.15 mm fixed gap). All rheological experiments were performed in triplicate to ensure reproducibility. Before fiber embedding, the printability of the bioink was evaluated as a function of ALG/Gel total polymer concentration (6, 8, and 10% w/v). A temperature sweep test was performed to assess printing performance by gradually increasing the temperature from 20 to 40°C at a rate of 1.5°C/min (frequency: 1 Hz; strain: 1%) while monitoring the viscoelastic properties (i.e., storage modulus, loss modulus, and complex viscosity). To determine shear-thinning properties, viscosity profiles of hydrogel precursor solutions were obtained using a continuously ramped shear rate (0.01–1,000 $s^{-1}$). To quantitatively assess shear-thinning behavior, a power-law model was applied

$$\eta(\dot{g}) = K \times \dot{g}^{(n-1)} \quad (1)$$

where $\eta$ is the viscosity, $\dot{g}$ is the shear rate, $K$ is the consistency index (viscosity at the shear rate of 1 $s^{-1}$), and $n$ is the shear-thinning index. The analysis was conducted on ALG/Gel as well as fibrous formulations containing 1% and 2% w/v f-GFs (f-ALG/Gel [1%] and f-ALG/Gel [2%]). The $n$ index was derived from the slope (angular coefficient [m]) of the viscosity-shear rate plot. Specifically, a linear fitting function was used, and $n$ was calculated ($n = m + 1$) while K was defined from the intercept (c) as $K = 10^c$. Before analysis, samples (2 mm height) were soaked in PBS at 37°C for 180 s to ensure thermal equilibration. A solvent

trap filled with ultrapure water was used during the tests to prevent hydrogel drying. For this analysis, an angular frequency range of 0.1–100 rad/s was used, along with a constant nondestructive strain of 1.0%, as determined from the preliminary assessment of the sample's linear viscoelastic region. The effect of dual crosslinking ($CaCl_2$ + mTG) and fiber concentration (1% and 2%) was evaluated through frequency sweep tests performed on 2 mm-height samples at a constant strain of 1%, varying the frequency from 0.1 to 100 rad/s.

#### 2.5.2. Wet weight ratio under physiological conditions

To investigate the effects of dual crosslinking on wet weight under physiological conditions, ALG/Gel and f-ALG/Gel hydrogels (120 µL each) were immersed in 500 µL of PBS containing 0.1% $CaCl_2$. Samples ($n = 4$ for each formulation) were incubated at 37°C, and the solution was refreshed every 2–3 days to mimic cell culture conditions and prevent the accumulation of released materials. At specific time points (0, 1, 3, 5, 7, 14, 21, and 28 days), the wet weight was recorded, ensuring precise measurement by carefully removing the supernatant solution. The hydrogel wet weight ratio percentage was calculated using the following equation

$$Percentage\,wet\,weight\,ratio\left(\%\right)=\frac{wf}{wi}\times 100 \qquad (2)$$

where $w_f$ and $w_i$ are the weight of the wet hydrogel on the 5th day and day 0, respectively.

#### 2.5.3. Mechanical characterization

Compression tests were carried out on crosslinked hydrogels to determine the mTG concentration (2.5%, 5%, and 10% w/v) and fiber density (0%, 1%, and 2% w/v) that best reproduced SMT mechanical properties. Uniaxial compressive tests were then performed on optimized hydrogel compositions (polymer final concentration, fiber density, and mTG percentage) immediately after sample production and following a 24-h incubation in PBS at 37°C. Cylindrical samples ($n = 4$) with a regular geometry were prepared by casting 200 µL of hydrogel into a 48-well plate. The compression tests were conducted using the MTS QTest/10 system (MTS Systems S.r.l., Italy) equipped with the Testwork 4 software (MTS Systems S.r.l., Italy). A 10 N load cell and a test speed of 1 mm/min were used for all measurements. Each test was automatically stopped by the Testwork 4 software when the applied load reached the load cell's maximum limit of 10 N. The engineering compressive stress (σ) was calculated using the following equation

$$\sigma=\frac{F}{\pi\times r^2} \qquad (3)$$

where $r$ represents the original radius of the specimen. The engineering strain ($\varepsilon$) under compression was defined as the percentage change in the specimen's thickness relative to its original thickness. Stress and strain values between 0% and 10% of $\varepsilon$ were used to determine the initial compressive modulus (E).

Unless otherwise specified, the term f-ALG/Gel will hereafter refer to the optimized formulation consisting of 6% w/v ALG/Gel (30:70 w/w),[25] supplemented with 2% w/v f-GFs and crosslinked using 2.5% w/v mTG.

### 2.6. 3D printing of fibrous microfilaments

The precursors ALG/Gel and f-ALG/Gel were microextruded using the R-GEN 200 printing station (REGENHU, 3D Discovery, Switzerland). ALG/Gel and f-ALG/Gel inks were loaded into a 3 mL bioprinting cartridge using a Luer-lock coupler and kept at 34°C before printing. The loaded cartridges were fitted with a 250 µm (34 Gauge, inner diameter) conical nozzle, and the whole setting was placed in the printing head. The layer height was set at 80% of the needle diameter (0.20 mm). Pressure was kept within the range of 25–30 kPa, and the feed rate was varied from 16 to 27 mm/s.[25] After constructs were printed, crosslinking was carried out by incubating them in mTG + $Ca^{2+}$ solution as described above. A specific aligned pattern, based on consecutive layers of long parallel microfilaments, was created using BioCAD software (REGENHU, Switzerland), to reproduce the arrangement of muscle bundles *in vivo*. To evaluate f-GF alignment, one layer with aligned patterns was printed on a glass slide at different feed rates (16, 20, and 27 mm/s), and samples were imaged in brightfield (Spinning Disk Nikon Crest Optics Ti2-E_X-Light V3, Nikon, Japan) at high magnifications (60× or 100×) to detect fiber distribution.

### 2.7. 3D printing of model square grid-shaped scaffolds to assess shape fidelity

To evaluate shape fidelity after printing, square grids (15 mm side, 3 mm spacing) were designed and printed at three different feed rates: 16, 20, and 27 mm/s. The printability index (PI) was used as a quantitative measure to assess printing at increasing speeds. For each experimental group, three pores from one-layer grid structures were imaged using a brightfield microscope (4× magnification; A1 HD25, Nikon, Japan). The resulting images were analyzed using a custom-made MATLAB script to calculate the PI according to the following equation

$$PI=\frac{L^2}{16\times A} \qquad (4)$$

where $L$ is the pore perimeter and $A$ is the pore area.

### 2.8. C2C12 cell maintenance

The C2C12 murine myoblasts (derived from satellite cells) were expanded in cell culture flasks using a growth medium composed of DMEM, 10% FBS, 1% penicillin/streptomycin, and 2% *L*-glutamine. Cells were maintained at 37°C in a humid atmosphere with 5% $CO_2$. To generate cell pellets for *in vitro* experiments, C2C12 cells were washed with PBS and removed from the culture flasks using 0.25% trypsin–EDTA (Thermo Fisher Scientific, US). The cell number was determined using a Neubauer hemocytometer. Next, the C2C12 cells were diluted to the desired amount and centrifuged at 900 rpm for 5 min.

### 2.9. Biological validation

Before cell culture, GFs were sterilized through immersion in 70% (v/v) ethanol for 1 h, PBS rinsing (two times), and UV treatment (30 min). To preliminarily study the interaction with GFs, C2C12 cells were seeded ($5 \times 10^3$ cells/cm$^2$) onto GFs and control tissue culture-treated polystyrene 24-well plates (control) and cultured for 7 days in growth medium. Prior to bioprinting, to assess hydrogel suitability for 3D cell encapsulation, 3D cell cultures were carried out by embedding C2C12 cells into 120 µL of ALG/Gel and f-ALG/Gel hydrogels ($5 \times 10^6$ cells/mL). Specifically, the cell pellet was first resuspended in the available volume of diluent (DMEM), then Gel volume was added, and the appropriate volume of ALG was measured using a precision syringe. The entire system (bioink) was gently mixed with a gel pipette, avoiding excessive stress on the cells and promoting their homogeneous dispersion within the final system. After constructs were cast, they were dual-crosslinked as explained in **Section 2.4.**, and washed three times with HBSS prior to the addition of cell culture media. Cells were cultured for 7 days in growth medium.

After 7 days of culture, C2C12 cells were washed with HBSS and fixed for 15 min in 4% paraformaldehyde (PFA) in PBS. Subsequently, the samples were washed three times in PBS and incubated in the dark in a PBS solution containing 4′,6-diamidino-2-phenylindole (DAPI; 1:1000 in PBS; Invitrogen, US) and phalloidin (rhodamine phalloidin F-actin, 1:1000 in PBS; Thermo Fisher Scientific, US). 3D-printed anisotropic constructs were prepared by loading ALG/Gel or f-ALG/Gel bioinks into a 5 mL cartridge, which was then placed in the printing head preheated to 33–35°C for 15 min. Typically, the printing head temperature was maintained at 33–35°C during the whole printing process. All prints were completed at RT under aseptic conditions.

The conical nozzle was calibrated on 3-(trimethoxysilyl) propyl methacrylate (TMSPMA)-coated glass slides prior to positioning a 24-well plate on the printing sample holder. Following computer-aided design (CAD; BioCAD software) and microextrusion parameter optimization, 3D-aligned C2C12 cell-laden structures were printed at a speed of 27 mm/s and a pressure of 25–30 kPa. At least six replicates for each composition ($n \geq 6$) were extruded through a 34-gauge nozzle. After the constructs were printed, they were dual crosslinked as explained in **Section 2.4.** and were washed three times with HBSS prior to the addition of cell culture media.

The 3D-printed cellular scaffolds were cultured for 14 days. Cell culture medium was replaced with fresh medium every 2–3 days. In detail, after 7 days in growth medium, the medium was replaced with a myoblast differentiation medium composed of DMEM, 2% horse serum (HS; Gibco, US), 1% penicillin/streptomycin, and 2% *L*-glutamine to promote musculoskeletal differentiation.[24] After 14 days of culture, C2C12 cells were washed with HBSS and fixed for 15 min in 4% PFA in PBS. Subsequently, three washes in PBS were performed, and cells were permeabilized with 0.1% Triton X-100 (Qiagen, Germany) solution. To block the nonspecific binding sites of antibodies, a solution of 1% w/v BSA was added and incubated for 1 h. Subsequently, cells were incubated overnight at 4°C in PBS–BSA (3:1 v/v) containing primary antibodies against skeletal fast myosin (1:200 in PBS; M1570, Sigma-Aldrich, US). After washing three times in PBS, samples were incubated in the dark with a PBS solution containing DAPI (1:1,000), phalloidin (1:1,000), and Alexa Fluor 647 anti-mouse secondary antibody (1:500, Invitrogen, US).

Samples were mounted on microscopy slides and observed under a fluorescence microscope (Nikon Eclipse Ti2 inverted microscope, Nikon, Japan). The quantification of myofiber organization was performed using a custom pipeline developed in MATLAB (R2024b, MathWorks, US). Immunofluorescence images were preprocessed through Gaussian filtering and adaptive contrast enhancement (CLAHE) to reduce noise while preserving edge information. Initial segmentation was performed using global thresholding, followed by morphological operations to clean and refine the detected structures. A watershed-based separation algorithm was applied to accurately identify individual instances of nuclei and fibers. Then, the segmented structures underwent morphological validation based on shape criteria (eccentricity, axial ratio, and area).

Quantitative analysis was performed to extract parameters characterizing tissue organization. The average fiber area was calculated from the segmented myosin-positive regions, providing a measure of muscle fiber size. Fiber length was computed through major axis analysis of the segmented regions, quantifying the longitudinal extension of myotubes. Fiber orientation was measured as

the angle between each fiber's major axis and the horizontal axis. The fusion index was determined as the ratio of nuclei within multinucleated myosin-positive myotubes (≥2 nuclei) to total nuclei.

Myogenic transcription factors were analyzed through droplet digital polymerase chain reaction (ddPCR) after 14 days of culture. Bioink-encapsulated cells (ALG/Gel and f-ALG/Gel) were extracted for RNA isolation through treatment with type 2 collagenase (255 U/mL; Worthington Biochemical Corporation, USA) for 45 min at 37°C, followed by trypsin–EDTA (0.25%, Gibco, US) for 5 min at 37°C to dissolve the gel. After treatment, samples were centrifuged at 400 × g for 10 min to collect the cells. Total RNA was isolated with TRIzol reagent (Invitrogen, US) following the manufacturer's instructions. RNA concentration and quality were assessed using the NanoQuant plate (Tecan Group Ltd, Switzerland). cDNA (200 ng) was obtained using the High-Capacity cDNA Reverse Transcription Kit (Applied Biosystems, US) following the manufacturer's protocol. ddPCR was performed to quantify the expression of myoblast determination protein 1 (*Myod1*; ID assay: dHsaCPE5052344) and myogenin (*Myog*; ID assay: qHsaCEP0050426) using ddPCR Supermix for probes without dUTP. Droplet generation was performed according to the manufacturer's instructions. Thermal-cycling conditions were 95°C for 10 min (1 cycle), 94°C for 30 s and 55°C for 30 s (40 cycles), 98°C for 10 min (1 cycle), and a 4°C infinite hold. Glyceraldehyde-3-phosphate dehydrogenase (*Gapdh*; ID assay: dHsaC-PE5031597) was used as a housekeeping gene for normalization. PCR plates were read on the Bio-Rad QX100 droplet reader (Bio-Rad Laboratories, US), and data were analyzed using the QuantaSoft analysis software (QX Manager v1.0 Standard Edition, Bio-Rad Laboratories, US). Results were reported as the concentration (cDNA copies per µL) of the gene of interest relative to *Gapdh*. No-template controls with water were included in each assay. Experiments were performed in triplicate and repeated twice. RNA samples of low quality were excluded from analysis.

### 2.10. Statistical analysis

Unless otherwise specified, all measurements were made in triplicate, and data are reported as mean values ± standard deviation (SD). Data were analyzed using one-way ANOVA when comparing multiple groups, and pairwise comparisons between two experimental groups were assessed using *t*-tests, all implemented in GraphPad Prism 9 (GraphPad Software, Inc., US). Tukey post hoc test was applied following ANOVA to identify significant differences between two or more groups. In particular, $*p < 0.05$, $**p < 0.01$, $***p < 0.001$, and $****p < 0.0001$ were considered statistically significant.

## 3. Results

### 3.1. Gelatin fiber production, fragmentation, and characterization

Using the electrospinning technique, GPTMS-crosslinked GFs were successfully fabricated. The morphology of the fibers was examined using SEM (Figure 1A). SEM images analyzed using the ImageJ software revealed an average fiber diameter of 425 ± 60nm. Fiber surface wettability was assessed via static contact angle measurements (Figure S1A), showing an average contact angle of 39° ± 2°. The angular speed of the collecting mandrel (3,800 rpm) promoted fiber alignment, as demonstrated by directionality histograms (ImageJ/FIJI), which exhibited a narrow, single-peak distribution (Figure S1B). GF biocompatibility was evaluated *in vitro* using C2C12 murine skeletal muscle cells cultured on GFs versus standard tissue culture plates. After 7 days, C2C12 cells were fixed and immunoassayed for myosin heavy chain (myosin), a key protein involved in myotube formation and SMT development (Figure 1B). GFs were found to promote C2C12 cell adhesion and structural organization compared to control, attributed to their ordered fibrous structure, supporting cell orientation, cell–cell interaction, and myoblast fusion. Furthermore, GFs induced a myogenic-like behavior in C2C12 cells, resulting in a pronounced expression of myosin compared to the control and promoting their organization into long, parallelly aligned myotubes with striated structures.

The GF mats were fragmented into separate short fibers (f-GFs) through mechanical homogenization, avoiding the use of chemical agents, and performed under ice cooling to minimize ductile fracture and prevent fiber aggregation. The method allowed accurate control over fiber length and morphology. Moreover, f-GFs were easily suspended in water without clustering. The fiber chemical composition before and after fragmentation was investigated through ATR-FTIR. In Figure 2C, the ATR-FTIR spectra of Gel powder, GFs, and f-GFs are presented. All spectra showed the characteristic bands of amide I at 1,633 $cm^{-1}$ (C=O stretching vibrations)[30] and amide II at 1,525 $cm^{-1}$ (N–H bending vibrations). Additionally, at 1,110 $cm^{-1}$, GFs and f-GFs spectra showed the characteristic band of Si–O–Si bonds,[31] confirming successful GPTMS-mediated crosslinking.[32] Furthermore, the peaks at 1,456 and 1,200 $cm^{-1}$ were due to $CH_2$ bending and $CH_3$ rocking vibrations of the siloxyalkyl group (Si–O–$CH_3$) in GPTMS, respectively.

### 3.2. Hydrogel characterization

The rheological behavior of the hydrogel precursors was initially assessed via temperature sweep and flow tests to evaluate their printability. As shown in Figure 3A and B, increasing the total polymer concentration from 6% to

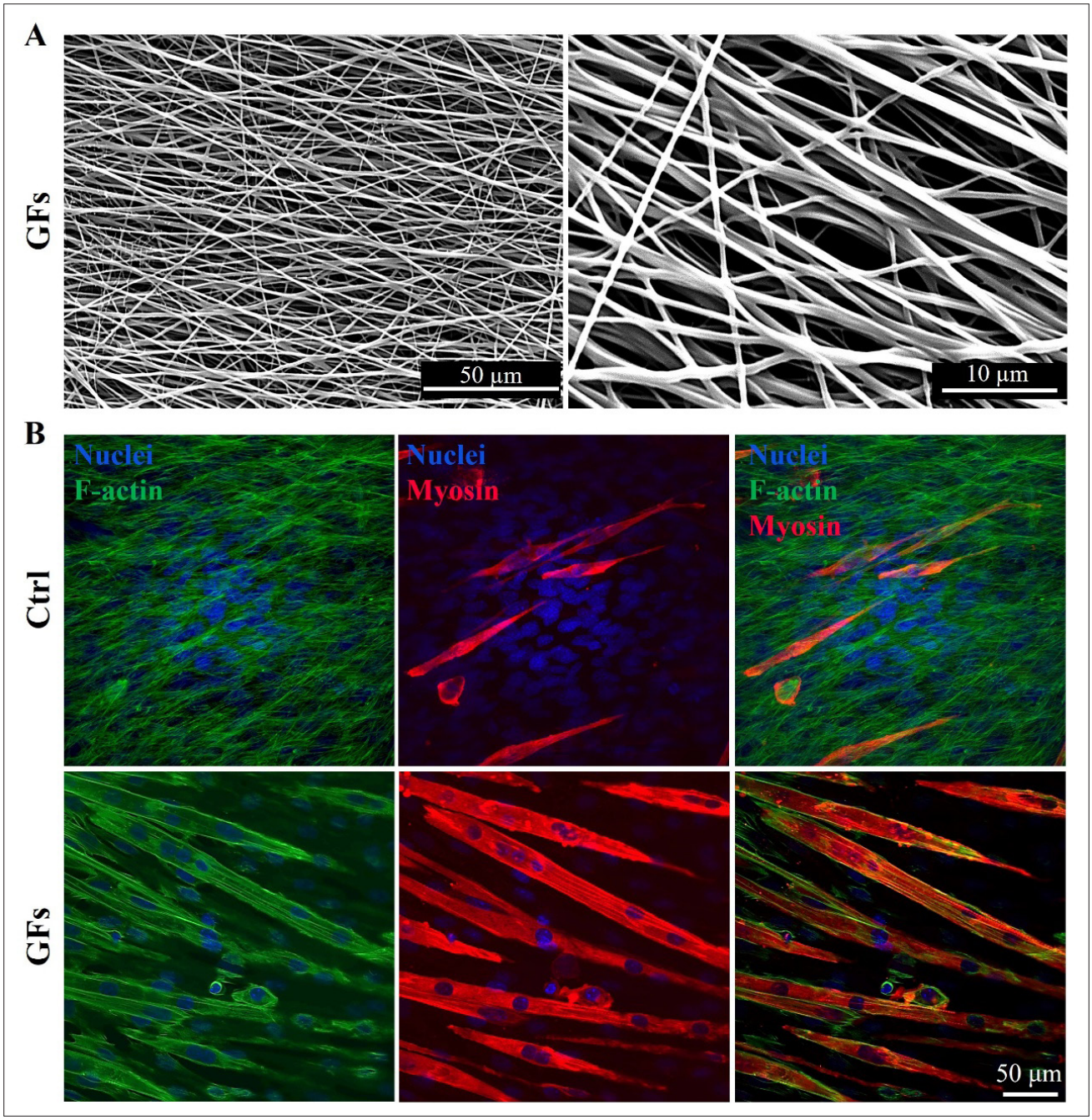


**Figure 1.** Gelatin fiber (GF) characterization and biological validation. (A) Scanning electron microscopy images of GFs at different magnifications. Scale bars: 10 μm; magnifications: 5000× (left), 10,000× (right). (B) Immunofluorescence images after 7 days of C2C12 cell culture on controls and GFs. Myosin in red, nuclei in blue, and F-actin in green. Scale bars: 50 μm; magnifications: 60×.

10% w/v led to higher viscosity and viscoelastic moduli across the tested temperature range (20–40°C). However, formulations with 8% and 10% polymer content exhibited excessively high viscosities and rapid loss of structural integrity near physiological temperature (~33°C), resulting in unstable flow and impaired extrusion performance. Due to these limitations, the 6% ALG/Gel formulation, exhibiting more favorable viscosity and thermal response, was selected as the bulk ink for further incorporation of f-GFs and subsequent characterization.

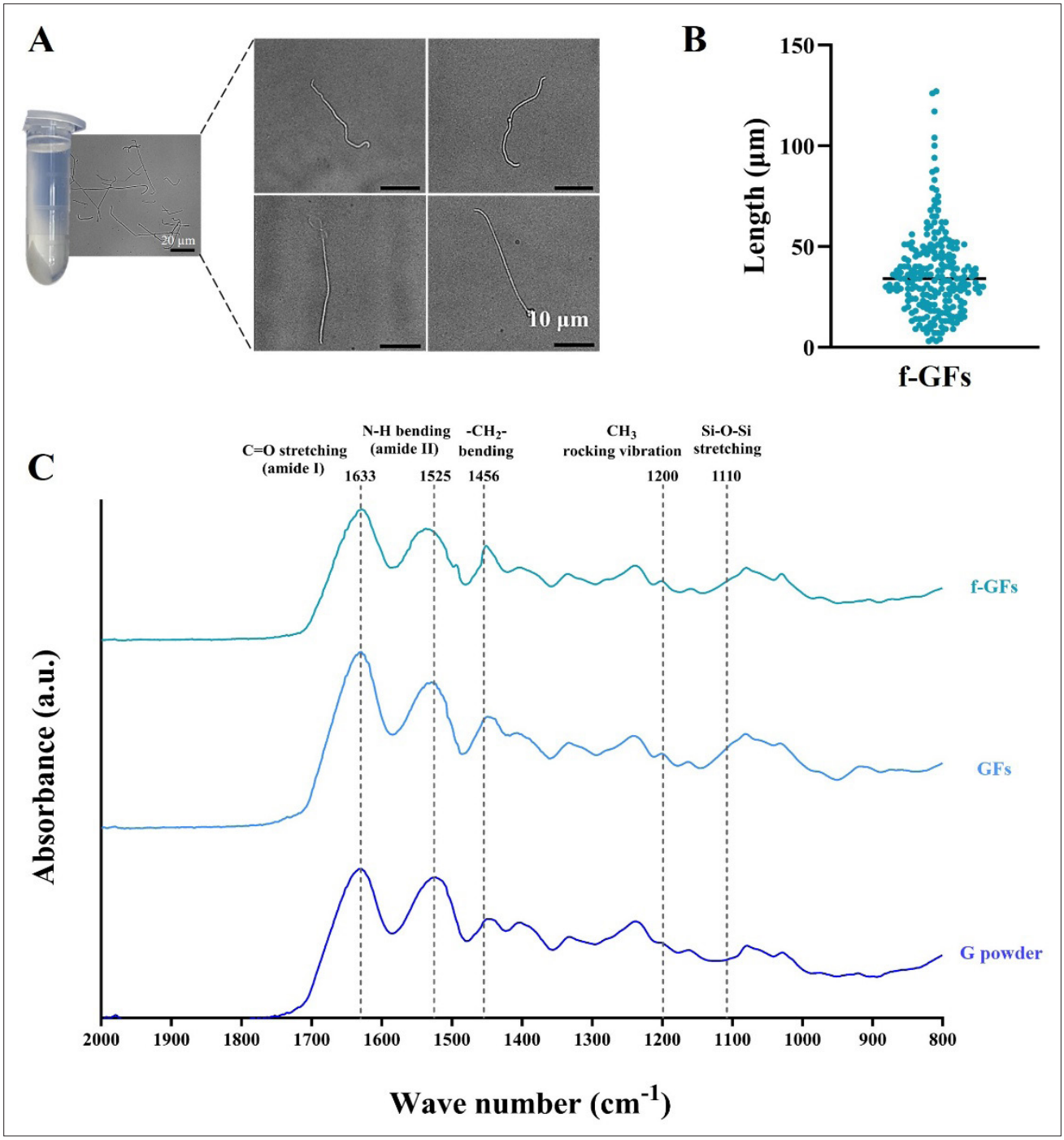


**Figure 2.** Characterization of fragmented gelatin fibers (f-GFs). (A) Pellet collecting and brightfield microscope images of f-GFs. Scale bar: 20 µm (left panel), 10 µm (right panel); magnifications: 20× (left panel), 60× (right panel). (B) Length distribution analysis, plotting individual values and their median. Range: 0–130 µm. (C) Attenuated total reflectance-Fourier transform infrared spectroscopy (ATR-FTIR) spectra of gelatin powder (G powder), GFs, and f-GFs, showing gelatin-related absorption bands for all samples and GPTMS-related absorption bands for GFs and f-GFs.

To evaluate the influence of fiber density on shear-thinning behavior, viscosity profiles were recorded at 33°C under a continuously ramped shear rate (0.01–1,000 $s^{-1}$) for ALG/Gel and f-ALG/Gel precursors containing 1% and 2% f-GFs (Figure 3C). All formulations exhibited non-Newtonian, shear-thinning behavior. Notably, f-ALG/Gel samples displayed higher viscosity at low shear rates (<10 $s^{-1}$), potentially due to the presence of fibrous elements contributing to a more entangled network, while viscosity values converged across all groups at higher shear rates (10–1,000 $s^{-1}$).

Shear-thinning indices (n) were derived from the slope of the log–log viscosity vs. shear rate curve using the power-law model (Figure 3D). All $n$ values were <1, confirming shear-thinning behavior. f-ALG/Gel inks presented significantly lower $n$ values (0.31 ± 0.03 for 2% f-GFs; 0.68 ± 0.05 for 1% f-GFs) compared to ALG/Gel (0.81 ± 0.02), indicating a more pronounced shear-thinning effect that enhances shape fidelity during printing. F-GFs (0%, 1%, and 2% w/v) were incorporated into ALG/Gel hydrogel precursors and subjected to dual crosslinking. ALG was crosslinked through $CaCl_2$ addition (0.1 M), leading to calcium ion complexation of glucuronic acid units. Enzymatic crosslinking was carried out using mTG (2.5%, 5%, or 10% w/v), promoting the formation of isopeptide bonds between the side-chain amide groups of glutamine residues and ε-amino groups of lysine residues.

To optimize the crosslinking conditions of ALG/Gel hydrogels, we evaluated the effects of varying the duration of ionic crosslinking with 0.1 M $CaCl_2$ (15 vs. 30 min) and the concentration of enzymatic crosslinking with mTG at 2.5%, 5%, or 10% w/v. Mechanical testing revealed that higher mTG concentrations (5% and 10% w/v) resulted in excessive stiffening, compromising the biomimetic compliance of the hydrogels. Consequently, the combination of 0.1 M $CaCl_2$ for 15 min and 2.5% mTG was selected as the optimal crosslinking condition for subsequent experiments (Figure S2A–D).

To further assess fiber density influence on viscoelastic properties, frequency sweep tests were performed on dual crosslinked hydrogels ($Ca^{2+}$ = 0.1 M-15 min + mTG = 2.5% w/v; Figure 3E). All groups exhibited $G'>G''$ across the frequency range (0.1–100 rad/s), consistent with a predominantly elastic behavior. The addition of f-GFs reinforced the hydrogel network, as evidenced by the increased $G'$ values. At 1 rad/s, $G'$ was significantly higher for f-ALG/Gel (2%; 11,900 ± 436 Pa) compared to f-ALG/Gel (1%; 9,180 ± 670 Pa) and ALG/Gel (9,960 ± 240 Pa) (Figure 3F). No statistical difference was observed between f-ALG/Gel (1%) and ALG/Gel.

Next, uniaxial compression tests were conducted to evaluate the mechanical performance of the hydrogels after fiber embedding (Figure 3G and H). The stress–strain profiles showed greater resistance to deformation with increasing fiber content. Young's modulus, derived from the linear region of the curve (Figure 3H), confirmed enhanced stiffness with f-GFs incorporation: 8.1 ± 1.3 kPa for ALG/Gel, 11.5 ± 3.8 kPa for f-ALG/Gel (1%), and 18.3 ± 2.9 kPa for f-ALG/Gel (2%). No statistical difference was observed between f-ALG/Gel (1%) and ALG/Gel.

These findings support the ability of embedded fibers to reinforce the matrix and confer more biomimetic mechanical properties suitable for SMT engineering. Based on these results, the f-ALG/Gel formulation containing 2% w/v fibers was selected for subsequent experiments. For all cell-based assays, the nonfibrous ALG/Gel hydrogel was used as the experimental control. From this point forward, f-ALG/Gel was used to indicate the selected formulation composed of 6% w/v ALG/Gel (30:70 w/w), containing 2% w/v f-GFs and crosslinked with 2.5% w/v mTG, unless stated otherwise.

The SEM analysis of freeze-dried crosslinked ALG/Gel and f-ALG/Gel samples, fractured in liquid nitrogen, showed a similar porous structure. However, in f-ALG/Gel samples (Figure 4A), the pore walls exhibited fibrous features attributable to the embedded f-GFs. The percentage wet weight ratio of crosslinked ALG/Gel and f-ALG/Gel hydrogel samples in PBS at 37°C was investigated to provide information on their long-term stability in physiological conditions (Figure 4B). The temporal trend of wet weight percentage was similar for both hydrogels: an initial weight loss of around 25% was observed after 1–3 days, followed by a weight increase from 3 to 5 days, reaching 100% and settling at this value up to 10 days, then progressively decreasing from 15 to 28 days. At 28 days, f-ALG/Gel and ALG/Gel hydrogels were found to retain 83% and 73% of their initial wet weight, respectively.

Uniaxial compressive tests were performed on freshly prepared hydrogels and after 24 h of incubation in PBS at 37°C (Figure 4C and D). Compressive moduli were calculated as the slopes of the stress–strain curves in the initial linear zone (0–10%) (Figure 4C). The average moduli of f-ALG/Gel were significantly higher than those of ALG/Gel, both for freshly prepared hydrogels (18.3 ± 2.9 vs. 8.1 ± 1.3 kPa; $^{***}p < 0.001$) and samples incubated in PBS for 24 h (16.1 ± 1.7 vs. 6.4 ± 1.1 kPa; $^{****}p < 0.0001$). Notably, the mechanical properties of both ALG/Gel and f-ALG/Gel decreased after 24 h of incubation in PBS at 37°C (Figure 4D), attributed to their wet weight loss (Figure 4B).

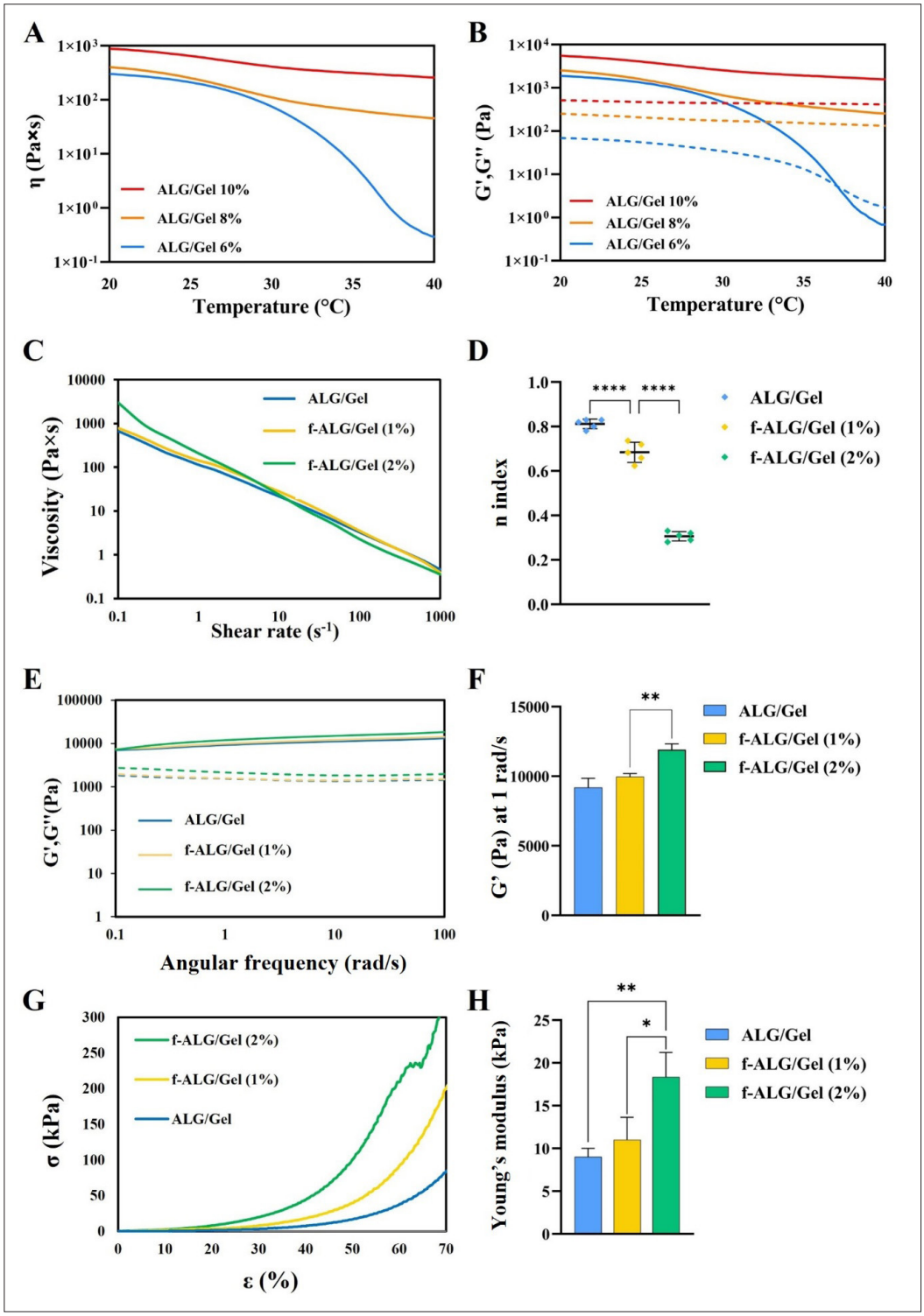


**Figure 3.** Rheological and mechanical characterization of ALG/Gel and f-ALG/Gel hydrogels. (A) Complex viscosity. (B) Storage (*G′*, solid lines) and loss (*G″*, dashed lines) moduli as a function of temperature (20–40°C, 1.5°C/min) of ALG/Gel formulations at 6%, 8%, and 10% w/v polymer concentration (ALG:Gel, 30:70 w/w; $n = 3$). (C) Viscosity profiles as a function of shear rate (0.01–1,000 $s^{-1}$) for optimized 6% w/v ALG/Gel and f-ALG/Gel bioinks with 1% and 2% w/v fiber content ($n = 3$). (D) Shear-thinning index (n) derived from power-law model fitting. (E) *G′* (solid lines) and *G″* (dashed lines) moduli as a function of frequency (0.1–100 rad/s) for dual-crosslinked hydrogels ($Ca^{2+}$/mTG; $n = 3$). (F) *G′* values obtained from frequency sweep tests at 1 rad/s ($n = 3$). (G) Representative stress–strain curves obtained from uniaxial compression tests. (H) Young's modulus derived from the linear region of the stress–strain curves ($n = 4$). Notes: $^{*}p < 0.05$, $^{**}p < 0.01$, $^{****}p < 0.0001$. Abbreviations: ALG, Alginate; f-ALG/Gel, alginate/gelatin with fibers; Gel, Gelatin.

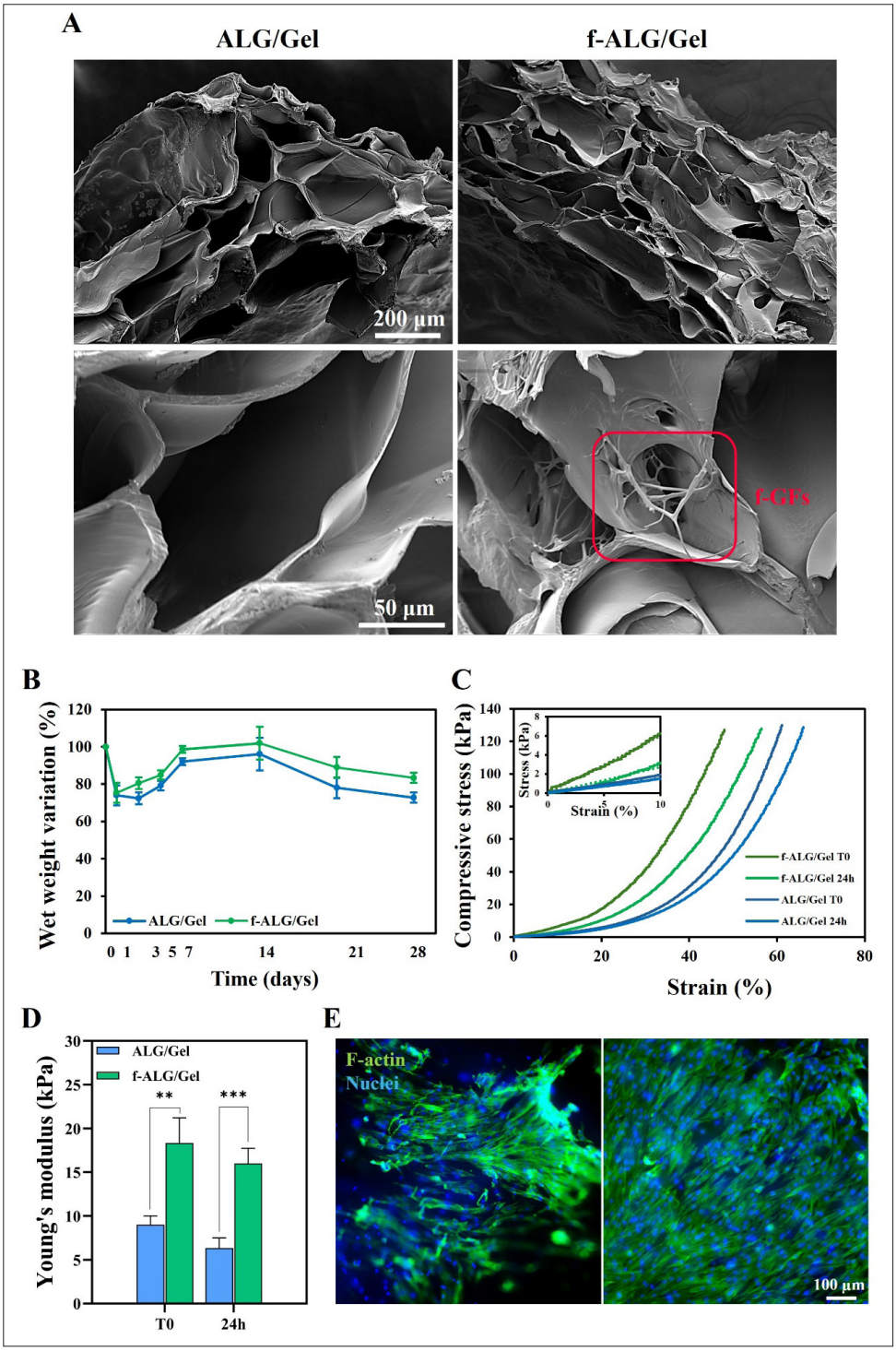


**Figure 4.** Characterization of optimized fibrous hydrogel. (A) Scanning electron microscopy images of ALG/Gel and f-ALG/Gel hydrogels after freeze-drying and brittle fracture in liquid nitrogen. Scale bars: 200 μm (upper panels), 50 μm (lower panels); magnifications: 300× (upper panels), 1500× (lower panels). (B) Wet weight variations of ALG/Gel and f-ALG/Gel hydrogels at 0, 1, 3, 5, 7, 14, 21, and 28 days of incubation in PBS at 37°C ($n = 4$). (C) Stress–strain (σ–ε%) curves from uniaxial compression tests for ALG/Gel and f-ALG/Gel hydrogels, performed after 0 day (freshly prepared) and after 1 day of incubation in PBS, and (D) corresponding Young's modulus values ($n = 6$). (E) Fluorescence images of C2C12 cells embedded into nonprinted ALG/Gel and f-ALG/Gel hydrogels and maintained in culture for 7 days, showing phalloidin staining of F-actin (green) and DAPI staining of nuclei (blue). Scale bars: 100 μm; magnifications: 20×. Notes: $^{**}p < 0.01$, $^{***}p < 0.001$ Abbreviations: ALG, Alginate; f-ALG/Gel, alginate/gelatin with fibers; Gel, Gelatin; PBS, Phosphate-buffered saline

Then, ALG/Gel and f-ALG/Gel hydrogels were characterized for their ability to support 3D cell culture. ALG/Gel and f-ALG/Gel hydrogels with embedded C2C12 cells were cultured in 24-well plates. After 7 days of culture, samples were stained for phalloidin/DAPI and analyzed under a confocal microscope (Figure 4E). Samples were analyzed at different z-planes (z-stack acquisition, 5 μm steps), showing a high density of cells with an elongated shape. These findings suggest that both hydrogels provided a suitable microenvironment for C2C12 cell culture.

### 3.3. 3D microextrusion printing optimization

The development of biomimetic 3D-printed anisotropic structures requires accurate control of scaffold geometry. To optimize microextrusion printing, model square grid-shaped structures of ALG/Gel and f-ALG/Gel were printed using a conical needle (inner diameter: 250 μm), at a pressure of 15–20 kPa, and three different printing speeds (16, 20, and 27 mm/s). The shape fidelity of the printed structures was assessed using the PI, calculated by analyzing pore geometry in brightfield microscopy images (4× magnification, $n = 5$; Figure 5A). The PI was determined by measuring the diameter and area of the grid pores, while pore circularity was evaluated using MATLAB software.

As shown in Figure 5B, PI < 1 indicates excessive filament spreading (poor printability), PI = 1 represents ideal printability with well-defined grid structures, and PI > 1 signifies filament gaps or breaks. For ALG/Gel, PI ranged from 0.93 to 0.96, indicating slight spreading of printed filaments. In contrast, f-ALG/Gel achieved PI values closer to 1.00, particularly at 20 and 27 mm/s, reflecting ideal printability and consistent grid formation. Based on these results, a printing speed of 27 mm/s was selected for 3D bioprinting.

To demonstrate the ability to extrude 3D structures with good shape retention, seven-layer grids were fabricated at the highest printing speed of 27 mm/s. As shown in Figure 5A (7 layers - 27 mm/s), the ALG/Gel system failed to maintain structural integrity, as the low viscosity causes the structure to collapse after the deposition of consecutive layers. In contrast, the f-ALG/Gel system supports the fabrication of stable 3D scaffolds, maintaining excellent geometric fidelity before crosslinking, aligning with the rheological data.

Next, to replicate the macro- and microarchitecture of SMT, characterized by bundles of muscle fibers, parallel hydrogel filaments were printed (Figure 5C). Optical microscopy images confirmed the printing of a uniform filament with an aligned structure. Additionally, embedded f-GFs showed a high degree of alignment along the filaments due to the applied shear stresses and filament postprinting crosslinking.

### 3.4. 3D fiber-embedded microextrusion bioprinting

Following printing parameter optimization, C2C12 cell-laden ALG/Gel and f-ALG/Gel bioinks were extruded into aligned 3D structures (Figure 6A) and maintained in culture for 14 days to promote cell spreading and organization within the engineered 3D microenvironments. *In vitro* cell culture was performed with/without HS addition to study the influence of combined biochemical and biophysical cues in inducing C2C12 cell differentiation and myotube maturation by assessing myofibrillar protein expression. As shown in Figure 6A, no detached cells with a round shape were detected upon F-actin staining. In contrast, in all conditions, C2C12 cells exhibited elongated shapes, suggesting successful cell adhesion and confirming the cytocompatibility of the bioprinting parameters.

To thoroughly investigate the effect of 3D topography on myoblast differentiation, immunofluorescence analysis of myosin heavy chain expression was performed after culturing the cells in contact with a proliferation or differentiation medium (HS supplemented) for 14 days. Limited myosin expression was observed for ALG/Gel constructs, with poorly aligned and scattered myotubes. Nuclei appeared dispersed, without clear alignment or clustering, indicating inefficient myoblast fusion. The addition of HS enhanced myosin expression, with some improvement in alignment and elongation of myotubes. However, the degree of myotube formation remained suboptimal. In contrast, f-ALG/Gel constructs showed unidirectional C2C12 cell growth along embedded GFs, with cells displaying elongated shape and cytoskeleton structure, significantly enhanced myosin expression, as well as well-aligned, elongated, and mature myotubes, as evidenced by the intense myosin staining and organized nuclei. The nuclei exhibited a more clustered and aligned organization, consistent with successful myoblast fusion and early-stage myotube formation under the 3D anisotropic stimulus without the need for further HS supplementation. *In vitro* C2C12 cell culture in 3D f-ALG/Gel constructs in the presence of HS led to a further significant increase in the formation of multinucleated myotubes with fiber-like morphologies.

Myogenic gene expression was quantified by ddPCR after 14 days of culture in ALG/Gel and f-ALG/Gel constructs (Figure 6B and C). A significant upregulation of *Myod1* mRNA expression was detected in f-ALG/Gel compared to ALG/Gel (**$p < 0.01$; Figure 6B), indicating increased activation of early myogenic pathways. Likewise, *Myog* expression was significantly higher in f-ALG/Gel (*$p$

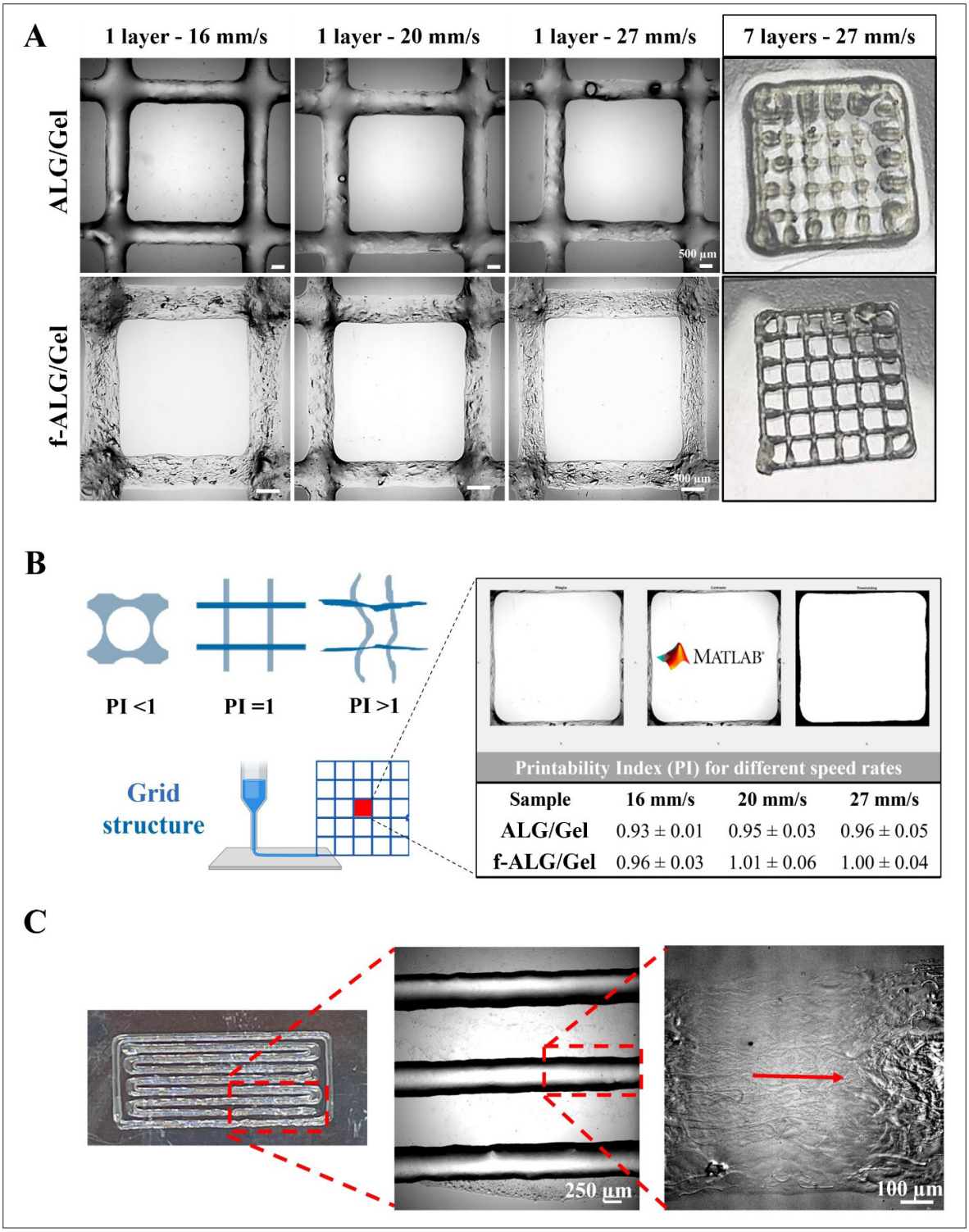


**Figure 5.** Microextrusion printing optimization. (A) Brightfield images of ALG/Gel and f-ALG/Gel square-grid structures, printed at a pressure of 25–30 kPa and increasing speed rates (16, 20, and 27 mm/s; $n = 4$; scale bars: 500 µm; magnifications: 4× [top panels], 4× [bottom panels]), and the macroscopic view of seven-layer printed constructs at 27 mm/s. (B) Schematic representation of printed grid-shaped structures with different PI values (left) and quantification of ALG/Gel and f-ALG/Gel hydrogel printability through PI at different speed rates (right). (C) Optical microscopy images at varying magnifications of the 3D-printed structures mimicking SMT architecture. The red arrow indicates the printing direction and fiber main orientation. Scale bars: 250 µm (middle panel), 100 µm (right panel); magnifications: 20× (middle panel), 60× (right panel). Abbreviations: ALG, Alginate; f-ALG/Gel, alginate/gelatin with fibers ; Gel, Gelatin; PI, Printability index; SMT, Skeletal muscle tissue.

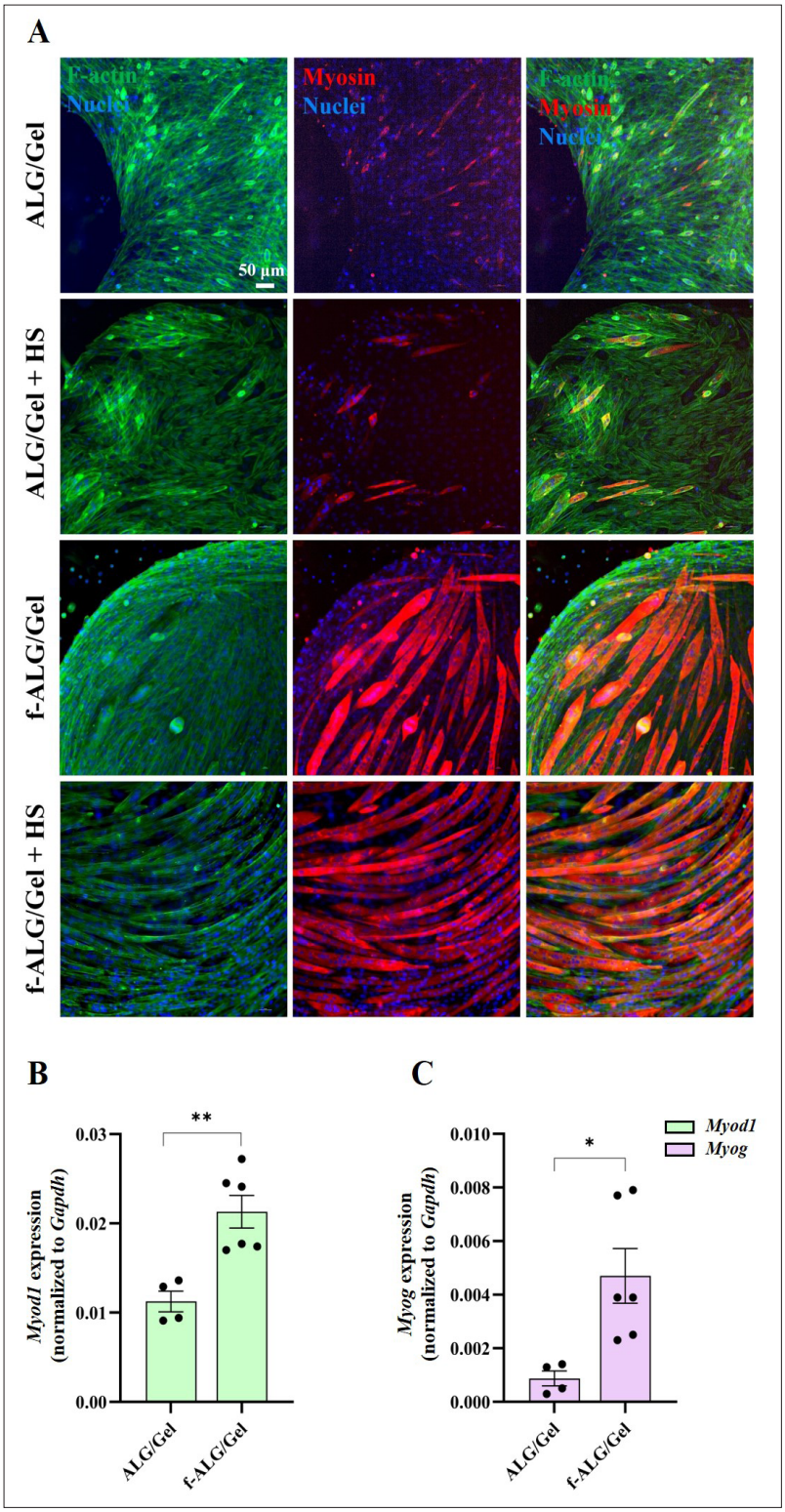


**Figure 6.** Characterization of C2C12 myogenic differentiation within ALG/Gel and f-ALG/Gel constructs. (A) Fluorescence microscopy images of myosin protein expression after 14 days of culture in the bioprinted scaffolds. Scale bars: 50 μm; magnifications: 40×. (B–C) ddPCR quantification of (B) *Myod* and (C) *Myog* mRNA expression normalized to *Gapdh*, showing enhanced activation of myogenic pathways in f-ALG/Gel. Notes: Data are presented as mean ± SEM ($n \geq 4$); *$p < 0.05$, **$p < 0.01$; unpaired *t*-test. Abbreviations: ALG, Alginate; ddPCR, Droplet digital polymerase chain reaction; f-ALG/Gel, alginate/gelatin with fibers; Gel, Gelatin; HS, Horse serum.

< 0.05; Figure 6C), confirming enhanced transcriptional activity of late myogenic markers.

Fluorescence microscopy images (Figure 7A) were analyzed using MATLAB software to derive four key metrics for the quantification of myotube organization and maturation: muscle fiber area, length, fusion index, and orientation variability (Figure 7B–E). In detail, the average values of myotube area, length, and fusion index, weighted by the total number of muscle fibers ($58 \leq n \leq 320$), were measured for each bioprinted construct from ≥5 independent images. 3D cell culture in bioprinted f-ALG/Gel scaffolds significantly enhanced muscle fiber properties compared to ALG/Gel scaffolds, including increased muscle fiber area (8,238 ± 2,848 vs. 3,317 ± 605 $\mu m^2$; Figure 7B), fiber length (306 ± 78 vs. 129 ± 22 μm; Figure 7C), and fusion index (27.8 ± 8.6% vs. 9.7 ± 0.9%; Figure 7D), while reducing muscle fiber orientation variability (Figure 7E).

By contrast, muscle fiber length did not change by 3D cell culture in bioprinted f-ALG/Gel scaffolds with additional HS stimulation (287 ± 41 μm), while HS increased muscle fiber length in cells cultured in bioprinted ALG/Gel scaffolds (153 ± 65 μm). Overall, these results suggest that biophysical cues through longitudinally oriented and cell-adhesive GFs embedded into f-ALG/Gel scaffolds significantly enhanced C2C12 cell spreading, differentiation, and fusion, leading to myotube formation, alignment, and maturation, compared to ALG/Gel scaffolds with/without further HS stimulation. The effect of the topographical biophysical cues was more pronounced than that of HS biochemical stimulation, demonstrating the key role of bioprinted fibrous scaffolds with anisotropic micro- and nanoscale organization in SMT engineering. The combination of biophysical cues with biochemical HS stimulation provided a synergistic effect in enhancing myotube differentiation, fusion, alignment, elongation, and maturation.

## 4. Discussion

The engineering of SMT aims to design functional tissue substitutes for regenerative medicine applications, such as replacement therapies and *in vitro* SMT models, and has recently gained attention as a promising strategy for cultured meat production.[6,7,33] To be effective, engineered scaffolds should closely replicate key biophysical features of native SMT, including its multiscale hierarchy,[34,35] mechanics, and contact guidance cues.[36] In this context, anisotropic substrates that mimic the nanoscale organization of collagen fibrils hold great potential.[37,38] While longitudinally oriented electrospun membranes can reproduce fibril morphology (260–410 nm in diameter),[16] they fail to capture the full 3D complexity of native SMT architecture, which plays a critical role in tissue functionality. This limitation highlights the need for advanced fabrication strategies capable of creating scaffolds that better emulate the structural and functional intricacies of native tissue. Developing 3D scaffolds that combine biomimetic anisotropy, appropriate mechanical properties, and cell-supportive environments remains a major challenge in the field. To address this gap, we designed a novel fibrous bioink for the bioprinting of 3D structures that replicate SMT anisotropy at both the nano- and microscale. This bioink consists of cell-adhesive GFs with nanometric dimensions embedded within a soft, cell-adhesive, shear-thinning hydrogel.

Regarding the fibrous component, electrospun GFs were prepared and mechanically fragmented via cryogenic milling to enable uniform dispersion within the hydrogel matrix. A-GFs with an average diameter of 425 ± 60 nm were prepared through electrospinning, closely matching the nanostructural characteristics of the native SMT ECM[16] (Figure 1A). Gel, a Food and Drug Administration-approved and cost-effective material derived from collagen,[39] was selected for its biocompatibility, biodegradability, and processability. Furthermore, Gel promotes cell adhesion due to the Arg–Gly–Asp (RGD) peptide motifs along its chains, which are fundamental for supporting the growth and differentiation of skeletal myoblasts.[40,41]

To enhance the mechanical stability of electrospun GFs, GPTMS was selected as a crosslinking agent owing to its well-established biocompatibility and proven efficacy in Gel-based systems.[42] GPTMS mediates covalent stabilization through epoxide–amine reactions and subsequent Si–O–Si condensation, thus improving aqueous resistance while preserving fibrous morphology. Unlike conventional postprocessing approaches,[22] GPTMS-mediated crosslinking occurs *in situ* during electrospinning and is completed after solvent evaporation, thereby preventing fiber swelling or partial dissolution and ensuring structural integrity.[26,27] This method avoids disruptive postprocessing steps and preserves fiber morphology. In addition, GPTMS does not alter the viscosity of the spinning solution, representing a further advantage compared with alternative crosslinkers, such as genipin. In this work, GPTMS was used at 1.84% v/v based on previous studies, showing excellent fiber stability and cytocompatibility with human fibroblasts. While higher concentrations (3–6% v/v) are commonly reported with proven cytocompatibility, our results suggest that effective crosslinking can be achieved at a lower dosage, reducing potential cytotoxicity and enhancing the translational relevance of the bioink under mild, cytocompatible conditions.

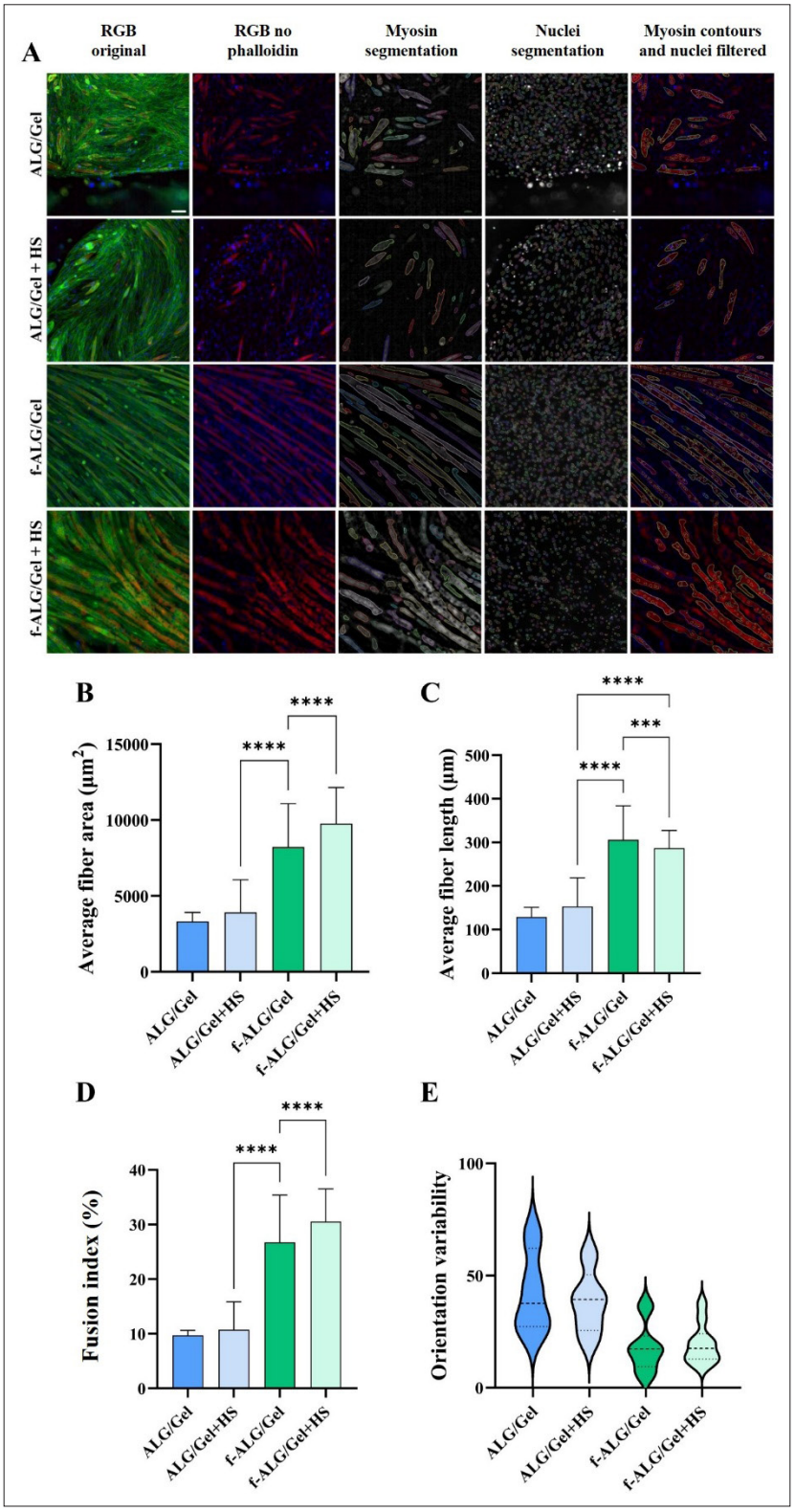


**Figure 7.** Image elaboration through Gaussian filtering and adaptive contrast enhancement (CLAHE). (A) Representative images from the custom pipeline developed in MATLAB. Scale bars: 50 μm; magnifications: 40×. (B) Average muscle fiber area. (C) Average fiber length. (D) Fusion index. (E) Orientation variability of myotubes, presented as violin plots. Notes: 58≤ *n* muscle fibers ≤320 from more than five independent images; Data are presented as mean ± standard deviation; ***$p < 0.001$; ****$p < 0.0001$. Abbreviations: ALG, Alginate; f-ALG/Gel, alginate/gelatin with fibers; Gel, Gelatin; HS, Horse

In this work, GPTMS-crosslinked GFs exhibited an intermediate wettability (Figure S1A), which preserved their ability to interact with the natural polymer components of the hydrogels while reducing inter-fiber interactions. Additionally, the electrospun membranes (GFs) with unidirectionally oriented morphology (directionality histograms; Figure S1B) showed the ability to impart contact guidance to C2C12 cells after 7 days of culture (Figure 1B). Compared to the control condition, cells cultured on GFs acquired an anisotropic organization, with parallel and elongated myotubes (showing high myosin expression). These findings are in agreement with previous reports suggesting that the orientation, size, and density of the substrate topographical cues play a significant role in skeletal muscle cell behavior. Specifically, previous reports have shown that cell attachment and alignment can be achieved by culturing cells on fibers with a diameter of approximately 500 nm,[43–45] confirming the morphological biomimicry of the herein obtained GFs, which had an average diameter of 425 ± 60 nm.

To favor brittle fracture and avoid heating during the process, GF fragmentation was performed by mechanical homogenization under ice cooling.[46,47] This method offers several advantages, including ease of application, short processing times, high yield, control over fragmented fiber size, and preservation of fiber diameter and surface morphology, as confirmed by brightfield microscopy images (Figure 2A and B). The topography of GFs (Figure S1B) reduced entanglements between adjacent fibers and facilitated their separation after milling. f-GFs showed an average length of <100 µm (Figure 2A and B), allowing their extrusion through the printing nozzle with a 250 µm diameter when embedded into a hydrogel bioink.

The ATR-FTIR spectra of GFs before and after fragmentation (Figure 2C) were similar, suggesting no alterations in their chemical composition during fragmentation. ALG/Gel (30:70 w/w) with 6% w/v total polymer content was selected based on previous experiments[25] and further validated through temperature sweep test analysis (Figure 3A and B) to meet printability requirements. Although 8% and 10% w/v compositions exhibited higher viscosity, their rapid gelation near physiological temperatures and excessively high resistance to flow impaired extrusion performance, making them unsuitable for bioprinting applications.

Gelatin was chosen as the primary hydrogel component for its cell-adhesive properties and its ability to interact with embedded f-GFs due to their similar composition.[46] ALG was introduced for its shear-thinning behavior and fast calcium-mediated gelation, making it a suitable component in bioinks for tissue engineering applications.[47] Notably, bioinks should support cell survival during and postprinting, ensure printability, and produce high-resolution, shape-stable 3D structures.[48] In this regard, polymer concentration plays a crucial role. Higher bioink concentrations enhance printing resolution and fidelity, but also increase shear stresses, potentially affecting cell viability.[49,50] Additionally, excessive polymer concentration and/or crosslinking density can limit nutrient diffusion and waste removal, restrict cell spreading postgelation, and hinder hydrogel remodeling by encapsulated cells, crucial for tissue maturation.[51] To address these challenges, shear-thinning bioinks with optimized viscosity and low polymer content have been proposed by incorporating small amounts of micro- or nanofillers (0.5–10% w/v),[52–54] thereby promoting cell viability and spreading in 3D microenvironments.

In this study, compared with previously published ALG/Gel bioinks,[55] the presence of a small amount (2% w/v) of f-GFs enabled precise printing of self-standing, cell-laden, 3D-aligned filaments, without the need for sacrificial layers, support baths, or high polymer concentration.[56,57] Herein, we demonstrated that the incorporation of f-GFs (2% w/v) into ALG/Gel hydrogels (6% w/v) significantly improved the ink's rheological properties (Figure 3C–F), potentially due to the formation of additional secondary interactions between ALG and Gel chains. At 33°C, f-ALG/Gel precursors (1% and 2% w/v) exhibited higher viscosity than ALG/Gel, particularly at low shear rates (<10 $s^{-1}$),[58] as shown in Figure 3C. Although all formulations exhibited shear-thinning behavior, this increase was more pronounced in the formulation containing 2% w/v f-GFs. The enhanced shear-thinning properties of f-ALG/Gel hydrogel precursors are critical not only for facilitating the printing process but also for promoting the alignment of embedded fibers within the printed filaments.[22,59] Additionally, f-ALG/Gel (2%) exhibited the lowest $n$ value (0.31 ± 0.03), indicating a stronger shear-thinning effect than the 1% formulation (0.68 ± 0.05), and a significantly improved performance compared to ALG/Gel (0.81 ± 0.02) (Figure 3D). These results suggest that increasing fiber content leads to a more entangled microstructure, enhancing printability by reducing viscosity more effectively under shear. f-ALG/Gel (1%) showed intermediate behavior, providing partial enhancement but less pronounced compared to f-ALG/Gel (2%), supporting the choice of the latter for optimal print fidelity and fiber organization during extrusion.

The enhancement in rheological properties observed in the f-ALG/Gel (2%) hydrogel precursors was retained following ionic and enzymatic crosslinking with calcium chloride and transglutaminase, respectively. Frequency-sweep tests (Figure 3E) revealed that $G'$ was consistently

higher than *G*" across the 1–100 Hz range, reflecting the solid-like behavior of both hydrogel formulations. Notably, both *G*' and *G*" values were higher for f-ALG/Gel formulations, indicating matrix reinforcement due to the incorporation of f-GFs. Particularly, at 1 rad/s, *G*' was significantly higher for f-ALG/Gel (2%) compared to f-ALG/Gel (1%) and ALG/Gel (Figure 3F), suggesting improved mechanical integrity. Similar results were reported by Kamaraj *et al*.,[23] who observed an increase in *G*'/*G*" at higher fiber concentrations compared to those used in this study. Compressive tests demonstrated that f-ALG/Gel (2%) effectively matched SMT mechanical properties (Figure 3G and H).

Overall, 2% w/v f-GFs showed the lowest shear-thinning index (0.31 ± 0.03), higher storage modulus, and a physiologically relevant Young's modulus (16.1 ± 1.7 kPa). Therefore, it was selected for the engineering of hierarchically aligned fibrous structures by microextrusion printing (Figure 4A). Unless otherwise specified, the term f-ALG/Gel will hereafter refer to the optimized formulation consisting of 6% w/v ALG/Gel (30:70 w/w), supplemented with 2% w/v f-GFs and crosslinked using 2.5% w/v mTG.

Traditional 2D cultures of C2C12 cells are generally unsuitable for long-term studies, as differentiated myotubes tend to detach from tissue culture polystyrene plates.[60,61] This limitation highlights the need for encapsulating cells within a 3D microenvironment to support their adhesion, maturation, and functional stability over time. To this end, the crosslinked f-ALG/Gel hydrogels were investigated for their stability under physiological conditions. The developed hydrogels exhibited an initial weight loss of approximately 20% during the first 24 h of incubation in PBS at 37°C (Figure 4B), potentially due to the release of unreacted materials. Additionally, they demonstrated excellent stability over a period of 28 days, enabling long-term cell culture supporting myotube formation and maturation.[62]

*In vitro* myogenic differentiation is markedly affected by the mechanical properties of the engineered biomaterial substrates. Therefore, the stiffness of freshly prepared f-ALG/Gel and ALG/Gel hydrogels was studied after 24 h of incubation in PBS to assess potential changes in mechanical behavior due to polymer release (Figure 3C and D). The incorporation of f-GFs significantly enhanced the compressive strength of hydrogels, in agreement with findings from frequency sweep tests. After 24 h of incubation in PBS, the Young's modulus was 6.3 ± 1.2 and 16.1 ± 1.7 kPa for ALG/Gel and f-ALG/Gel hydrogels, respectively, confirming that the stiffness of f-ALG/Gel falls within the physiological range of SMT (10–60 kPa).[63] Based on the literature, f-ALG/Gel stiffness results are optimal for promoting myotube formation. Consistently, Engler *et al*.[64] previously demonstrated that the maturation of myotubes is enhanced on hydrogels with a physiological Young's modulus of approximately 12 kPa. Overall, f-ALG/Gel hydrogels reproduced key biophysical features of SMT, including a fibrous structure that promotes contact guidance and tissue-like mechanical stiffness. ALG/Gel and f-ALG/Gel bulk hydrogels were initially investigated for their suitability for 3D C2C12 cell encapsulation (Figure 3E). Following 7 days of culture, phalloidin/DAPI staining demonstrated excellent 3D cell colonization, spreading, and organization for both formulations, confirming hydrogel bioactivity. Qualitatively, higher cell proliferation was observed in the f-ALG/Gel system. Next, the printability of f-ALG/Gel was evaluated, with a focus on exploiting shear stresses to promote f-GF alignment. Importantly, the selected f-GF concentration did not cause needle clogging during microextrusion. Recent studies have shown that the introduction of homogeneously dispersed short silk or nanocellulose fibers into hydrogels can strongly enhance their printability. As previously underlined, fibrous fillers increase the bioink viscosity at low shear rates through the establishment of physical interactions with hydrogel polymer components,[52,65,66] improving printability and shape fidelity postprinting. Shape fidelity indicates that the printed geometries closely match the original CAD design and preserve their structure postprinting.[67] In this work, the nonlinear rheological properties and enhanced stiffness of f-ALG/Gel inks (Figure 3) accounted for their continuous extrusion with minimal postextrusion swelling and spreading (Figure 5A). Shape fidelity was enhanced for f-ALG/Gel vs. ALG/Gel hydrogels (Figure 5B) across all tested printing speed rates (16, 20, and 27 mm/s), resulting in well-defined grid structures, particularly at 27 mm/s. This facilitated the formation of aligned-fiber-embedded 3D constructs, which were used to direct myoblast alignment, myogenesis, and myotube maturation, as shown in Figure 5C.

The optimized properties of f-ALG/Gel inks enabled the printing of self-supporting structures with a thickness ranging from 250 to 500 μm without the need for sacrificial materials or baths (Figure 5C). Postprinting, the rapid external crosslinking of the hydrogel precursors by calcium ions and mTG minimized die-swelling and preserving the shear-induced anisotropic structure. Following shear application, f-GF orientation was successfully achieved across the entire printed filaments within 3D aligned structures, as reported in Figures 5C and S3C. Shear stresses effectively aligned the embedded f-GFs along the printing direction, with the effect being particularly pronounced at a printing speed of 27 mm/s (Figure S3C). Fast gelation post-printing allowed the prompt stabilization of the

printed structures, including shear-induced alignment of embedded f-GFs. The dual crosslinking of ALG/Gel hydrogels was achieved upon 15 min of immersion in a solution containing $Ca^{2+}$ ions and mTG.[56]

Transglutaminase is an enzyme that catalyzes the formation of covalent bonds between protein chains, including Gel, and is widely used in regenerative medicine as well as in the food industry for improving the texture of processed meat products.[68] In this work, mTG was preferred over animal-derived enzymes due to its cost-effective production.[69] Postprinting crosslinking ensured that the viscosity and physicochemical properties of the system were preserved.

Cell-laden scaffolds with anisotropic micro- and nanoscale SMT organization can be obtained by printing parallel microfilaments, embedding aligned nanosized f-GFs. Following microextrusion and cell encapsulation optimization, 3D bioprinting was carried out to design cellular structures that capture the complexity of SMT *in vivo*, as shown in Figure 6A.

The degree of myogenesis and maturation in response to substrate biophysical cues was investigated by marking myosin, a key protein involved in SMT development. ALG/Gel and f-ALG/Gel 3D-printed aligned scaffolds successfully supported C2C12 cell growth. In ALG/Gel hydrogels, C2C12 cells exhibited isotropic spreading, with F-actin filaments extending in all directions, consistent with the absence of topographical cues. The lack of preferential orientation decreased cell differentiation and myotube maturation, as suggested by the weak expression of myosin protein. These results demonstrate that the bioprinting process alone was insufficient to induce cell anisotropy and efficient differentiation.

In contrast, immunofluorescence analysis of 3D-bioprinted f-ALG/Gel constructs (Figure 6A) showed the formation of packed and elongated myotubes with a mature structure, oriented along the microfilaments. The upregulation of *Myod1* (Figure 6B) and *Myog* (Figure 6C) in f-ALG/Gel hydrogels confirms the enhanced activation of the myogenic pathway promoted through the fibrous reinforcement. *Myod1* is a master regulator of myogenesis, whose expression is initiated upon myoblast activation and sustained during proliferation and early differentiation phases, promoting withdrawal from the cell cycle and commitment toward the myogenic lineage.[70] Conversely, *Myog* is specifically associated with late-stage differentiation and myotube maturation.[71] A similar sequential upregulation of *Myod1* and *Myog* has been observed in other biomimetic hydrogel systems supporting myoblast alignment and fusion,[72] reflecting the physiological transition of activated progenitors toward terminal differentiation. These findings are consistent with the enhanced myosin expression observed using immunofluorescence, suggesting that the anisotropic fibrous microarchitecture provides topographical and mechanical cues that promote full myogenic maturation of encapsulated cells.

The effect of anisotropic microenvironmental cues on C2C12 cell morphology, phenotype, and directional growth was quantified by immunofluorescence image analysis (Figure 7). The pipeline for image analysis employed Gaussian filtering and CLAHE to enhance contrast and reduce noise while preserving edge information. In this study, initial segmentation was performed using global thresholding, followed by morphological operations to refine detected structures. A watershed-based algorithm was then applied to separate overlapping features, ensuring accurate identification of nuclei and fibers. Morphological validation using shape parameters (eccentricity, axial ratio, and area) further ensured segmentation accuracy. Such approaches, inspired by advanced contrast enhancement and segmentation techniques, emphasize robustness in biomedical image processing, balancing noise reduction with detail preservation for precise analysis.

The 3D-bioprinted f-ALG/Gel scaffolds significantly improved C2C12 cell fusion (fusion index) and 3D myogenic differentiation (myotube length and spreading area). Particularly, previous publications[73] reported an F-actin coverage per cell of up to 615 $\mu m^2$; in this work, we demonstrated the formation of more elongated myotubes with an average area of 8,498 $\mu m^2$ for ALG/Gel and 10,014 $\mu m^2$ for f-ALG/Gel. These results confirmed the ability of 3D topographical cues to regulate C2C12 cell spatial arrangement and myotube organization without the need for mechanical or electrical stimulation. Similar results were achieved in the literature exploiting fiber-reinforced systems; however, they required longer culture times (≥ 21 days) to achieve an adequate degree of myogenesis and maturation.[74] Indeed, regarding the recently proposed silk fiber-reinforced bioinks for SMT engineering,[23] the currently proposed f-ALG/Gel hydrogels showed superior biomimicry due to the presence of GFs, resembling tissue-like collagen fibers. Recent literature has already shown that Gel-based fibers efficiently support C2C12 viability during *in vitro* culture and stimulate their differentiation, as suggested by the expression of myogenic regulatory factors.[40,41]

Overall, the bioprinted f-ALG/Gel scaffolds were found to provide an optimal microenvironment for C2C12 cell culture, differentiation, and myotube maturation, attributed to their biomimetic fibrous micro-/nanostructure, mechanical stiffness, and stability in

physiological conditions. Bioprinted f-ALG/Gel-based constructs showed great promise for SMT engineering because they guided the uniaxial arrangement of C2C12 cells, which is critical for achieving cell maturation.

The developed platform demonstrates high versatility and holds significant potential for a range of future applications, including *in vivo* tissue regeneration, *in vitro* models, and the engineering of cultured meat, all of which require further investigation. In future studies, the currently employed C2C12 murine myoblast cells can be replaced with hiPSC-derived skeletal muscle cells for regenerative medicine and *in vitro* SMT modeling, or with animal-derived skeletal muscle cells for cultured meat production. By incorporating f-GFs, the approach can be extended to a variety of natural and synthetic polymers, making it suitable not only for skeletal muscle but also for other aligned tissues. These fibers can also be tailored to specific cell types by including cell-interactive proteins (e.g., laminin) to enhance tissue-specific functionality. In terms of *in vivo* degradation, the system contains a high proportion of Gel, a component readily susceptible to enzymatic degradation, and its rate can be tailored through controlled crosslinking. As ALG is not inherently degradable, it could be replaced with ALG dialdehyde, where the degree of oxidation and molecular weight can be modulated to achieve tunable biodegradability.[25] Finally, the platform is also well-suited for strategies to promote vascularization, either through the incorporation of growth factors, such as vascular endothelial growth factor, into the bioink to stimulate *in situ* vessel formation, or by directly introducing vascularization through the printing of tubular vessel-like structures within the 3D constructs, exploiting the fibrous bioink to promote radial alignment of vascular smooth muscle cells.[24,75]

## 5. Conclusion

Innovative f-ALG/Gel bioinks were developed for the 3D bioprinting of anisotropic scaffolds that replicate the hierarchical micro- and nanoscale fibrous architecture, mechanical stiffness, and cell-supportive properties of SMT ECM. GF fragments served as hydrogel fillers, significantly enhancing bioink printability, the shape fidelity of printed constructs, and their mechanical stiffness. Such bioinks enabled the fabrication of self-supporting, cell-laden constructs without the need for sacrificial materials or supporting baths. Notably, the shear stress-induced anisotropic alignment of embedded fibers provided biomimetic biophysical cues that facilitated C2C12 cell adhesion, alignment, and differentiation into mature, parallelly aligned myotubes, closely mimicking the native structure of SMT. Furthermore, during bioink production, the preparation of GF fragments through cryogenic milling ensures scalability, while the avoidance of any potentially toxic agents and solvents provides an environmentally sustainable process. In the future, the substitution of C2C12 cells with primary human myoblasts or myogenic cells derived from hiPSCs will allow the engineering of human-relevant SMT. Human bioprinted constructs will be cultured for different durations, and functional SMT will be validated through contractility tests and calcium imaging assays. In parallel, the use of animal myoblasts will enable the application of this process to cultured meat engineering. In conclusion, a new class of structurally instructive bioinks has been designed by integrating advanced bioengineering strategies, showing significant promise for the bioprinting of next-generation SMT constructs with broad applications in regenerative medicine, *in vitro* SMT modeling, and the engineering of cultured meat.

## Acknowledgments

The authors thank Beatrice Francesca Massel and Francesca Sanna for their contributions to the *in vitro* modeling experiments as part of their Master's thesis research at the Politecnico di Torino.

## Funding

This work was supported by the European Research Council (ERC) under the European Union's Horizon 2020 Research and Innovation Programme (Grant Agreement No. 772168), through the BIORECAR ERC Consolidator project (www.biorecar.polito.it); and under the European Union's Research and Innovation Programme (Grant Agreement No. 101158332) for the ERC-2023-POC EMPATIC project.

## Conflict of interest

Elena Marcello serves as the Editorial Board Member of the journal, but did not in any way involve in the editorial and peer-review process conducted for this paper, directly or indirectly. Other authors declare they have no competing interests.

## Author contributions

*Conceptualization:* Gerardina Ruocco, Elena Marcello, Irene Carmagnola

*Data curation:* Gerardina Ruocco, Mattia Spedicati

*Formal analysis:* Gerardina Ruocco, Mattia Spedicati

*Funding acquisition:* Valeria Chiono

*Investigation:* Gerardina Ruocco, Elena Marcello, Irene Carmagnola, Valeria Chiono

*Methodology:* Gerardina Ruocco, Elena Marcello, Camilla Paoletti, Irene Carmagnola

*Project administration:* Irene Carmagnola, Valeria Chiono
*Resources:* Valeria Chiono
*Software:* Gerardina Ruocco, Massimo Salvi
*Supervision:* Elena Marcello, Camilla Paoletti, Alice Zoso, Irene Carmagnola, Valeria Chiono
*Validation:* Elena Marcello, Camilla Paoletti, Alice Zoso
*Writing–original draft:* Gerardina Ruocco, Massimo Salvi
*Writing–review & editing:* Elena Marcello, Irene Carmagnola, Valeria Chiono

## Ethics approval and consent to participate

Not applicable.

## Consent for publication

Not applicable.

## Availability of data

Data will be made available upon reasonable request to the corresponding author.

## Further disclosure

Part of the findings have been presented at the ESB2025 and Biofabrication conferences.

## References


1. Hulett NA, Scalzo RL, Reusch JEB. Glucose uptake by skeletal muscle within the contexts of type 2 diabetes and exercise: An integrated approach. *Nutrients*. 2022;14(3):647. doi: 10.3390/nu14030647
2. Kim J, Kim IU, Lee ZF, Sim G, Jeon JS. Strategic approaches in generation of robust microphysiological 3D musculoskeletal tissue system. *Adv Funct Mater*. 2024;34(52). doi: 10.1002/adfm.202410872
3. García-Lizarribar A, Villasante A, Lopez-Martin JA, *et al*. 3D bioprinted functional skeletal muscle models have potential applications for studies of muscle wasting in cancer cachexia. *Biomater Adv*. 2023;150:213426. doi: 10.1016/j.bioadv.2023.213426
4. Zhuang P, An J, Chua CK, Tan LP. Bioprinting of 3D in vitro skeletal muscle models: A review. *Mater Des*. 2020;193:108794. doi: 10.1016/j.matdes.2020.108794
5. Volpi M, Paradiso A, Costantini M, Święszkowski W. Hydrogel-based fiber biofabrication techniques for skeletal muscle tissue engineering. *ACS Biomater Sci Eng*. 2022;8(2):379-405. doi: 10.1021/acsbiomaterials.1c01145
6. Lou H, Lu H, Zhang S, *et al*. Highly aligned myotubes formation of piscine satellite cells in 3D fibrin hydrogels of cultured meat. *Int J Biol Macromol*. 2024;282:136879. doi: 10.1016/j.ijbiomac.2024.136879
7. Li X, Sim D, Wang Y, *et al*. Fiber-based biomaterial scaffolds for cell support towards the production of cultivated meat. *Acta Biomater*. 2025;191:292-307. doi: 10.1016/j.actbio.2024.11.006
8. Sabetkish S, Currie P, Meagher L. Recent trends in 3D bioprinting technology for skeletal muscle regeneration. *Acta Biomater*. 2024;181:46-66. doi: 10.1016/j.actbio.2024.04.038
9. Schwab A, Hélary C, Richards RG, Alini M, Eglin D, D'Este M. Tissue mimetic hyaluronan bioink containing collagen fibers with controlled orientation modulating cell migration and alignment. *Mater Today Bio*. 2020;7:100058. doi: 10.1016/j.mtbio.2020.100058
10. Mehmood H, Kasher PR, Barrett-Jolley R, Walmsley GL. Aligning with the 3Rs: Alternative models for research into muscle development and inherited myopathies. *BMC Vet Res*. 2024;20(1):477. doi: 10.1186/s12917-024-04309-z
11. Kang MS, Lee SH, Park WJ, Lee JE, Kim B, Han DW. Advanced techniques for skeletal muscle tissue engineering and regeneration. *Bioengineering*. 2020;7(3):99. doi: 10.3390/bioengineering7030099
12. Trovato F, Imbesi R, Conway N, Castrogiovanni P. Morphological and functional aspects of human skeletal muscle. *J Funct Morphol Kinesiol*. 2016;1(3):289-302. doi: 10.3390/jfmk1030289
13. Nikkhah M, Edalat F, Manoucheri S, Khademhosseini A. Engineering microscale topographies to control the cell–substrate interface. *Biomaterials*. 2012;33(21):5230-5246. doi: 10.1016/j.biomaterials.2012.03.079
14. Wang L, Wu Y, Guo B, Ma PX. Nanofiber yarn/hydrogel core–shell scaffolds mimicking native skeletal muscle tissue for guiding 3D myoblast alignment, elongation, and differentiation. *ACS Nano*. 2015;9(9):9167-9179. doi: 10.1021/acsnano.5b03644
15. Mueller C, Trujillo-Miranda M, Maier M, Heath DE, O'Connor AJ, Salehi S. Effects of external stimulators on engineered skeletal muscle tissue maturation. *Adv Mater Interfaces*. 2021;8(1). doi: 10.1002/admi.202001167
16. Ostrovidov S, Hosseini V, Ahadian S, *et al*. Skeletal muscle tissue engineering: Methods to form skeletal myotubes and their applications. *Tissue Eng Part B Rev*. 2014;20(5):403-436. doi: 10.1089/ten.teb.2013.0534
17. Kim H, Jang J, Park J, *et al*. Shear-induced alignment of collagen fibrils using 3D cell printing for corneal stroma tissue engineering. *Biofabrication*. 2019;11(3):035017. doi: 10.1088/1758-5090/ab1a8b
18. Moncal KK, Ozbolat V, Datta P, Heo DN, Ozbolat IT. Thermally-controlled extrusion-based bioprinting of collagen. *J Mater Sci Mater Med*. 2019;30(5):55.

doi: 10.1007/s10856-019-6258-2

19. Prendergast ME, Davidson MD, Burdick JA. A biofabrication method to align cells within bioprinted photocrosslinkable and cell-degradable hydrogel constructs via embedded fibers. *Biofabrication*. 2021;13(4). doi: 10.1088/1758-5090/AC25CC

20. Chaudhuri O, Cooper-White J, Janmey PA, Mooney DJ, Shenoy VB. Effects of extracellular matrix viscoelasticity on cellular behaviour. *Nature*. 2020;584(7822):535-546. doi: 10.1038/s41586-020-2612-2

21. Lloyd EM, Hepburn MS, Li J, *et al*. Multimodal three-dimensional characterization of murine skeletal muscle micro-scale elasticity, structure, and composition: Impact of dysferlinopathy, duchenne muscular dystrophy, and age on three hind-limb muscles. *J Mech Behav Biomed Mater*. 2024;160:106751. doi: 10.1016/j.jmbbm.2024.106751

22. Choi S, Lee KY, Kim SL, *et al*. Fibre-infused gel scaffolds guide cardiomyocyte alignment in 3d-printed ventricles. *Nat Mater*. 2023;22(8):1039-1046. doi: 10.1038/s41563-023-01611-3

23. Kamaraj M, Rezayof O, Barer A, *et al*. Development of silk microfiber-reinforced bioink for muscle tissue engineering and in situ printing by a handheld 3d printer. *Biomater Adv*. 2025;166:214057. doi: 10.1016/j.bioadv.2024.214057

24. Li T, Hou J, Wang L, *et al*. Bioprinted anisotropic scaffolds with fast stress relaxation bioink for engineering 3D skeletal muscle and repairing volumetric muscle loss. *Acta Biomater*. 2023;156:21-36. doi: 10.1016/j.actbio.2022.08.037

25. Stola GP, Paoletti C, Nicoletti L, *et al*. Internally-crosslinked alginate dialdehyde/alginate/gelatin-based hydrogels as bioinks for prospective cardiac tissue engineering applications. *Int J Bioprint*. 2024;10(6):544-566. doi: 10.36922/ijb.4014

26. Tonda-Turo C, Gentile P, Saracino S, *et al*. Comparative analysis of gelatin scaffolds crosslinked by genipin and silane coupling agent. *Int J Biol Macromol*. 2011;49(4):700-706. doi: 10.1016/j.ijbiomac.2011.07.002

27. Tonda-Turo C, Cipriani E, Gnavi S, *et al*. Crosslinked gelatin nanofibres: Preparation, characterisation and in vitro studies using glial-like cells. *Mater Sci Eng: C*. 2013;33(5):2723-2735. doi: 10.1016/j.msec.2013.02.039

28. Giuntoli G, Muzio G, Actis C, *et al*. In-vitro characterization of a hernia mesh featuring a nanostructured coating. *Front Bioeng Biotechnol*. 2021;8. doi: 10.3389/fbioe.2020.589223

29. John JV., McCarthy A, Wang H, *et al*. Engineering biomimetic nanofiber microspheres with tailored size, predesigned structure, and desired composition via gas bubble–mediated coaxial electrospray. *Small*. 2020;16(19). doi: 10.1002/smll.201907393

30. Carmagnola I, Chiono V, Ruocco G, *et al*. PLGA membranes functionalized with gelatin through biomimetic mussel-inspired strategy. *Nanomaterials*. 2020;10(11):2184. doi: 10.3390/nano10112184

31. Salgado-Delgado AM, González-Mondragón EG, Hernández-Pérez R, Salgado-Delgado R, Santana-Camilo JA, Olarte-Paredes A. Obtention and characterization of GO/Epoxy and GO-GPTMS/epoxy nanocompounds with different oxidation degrees and ultrasound methods. *C (Basel)*. 2023;9(1):28. doi: 10.3390/c9010028

32. Sitthiracha M, Kilmartin PA, Edmonds NR. Novel organic–inorganic hybrid materials based on epoxy-functionalized silanes. *J Solgel Sci Technol*. 2015;76(3):542-551. doi: 10.1007/s10971-015-3804-3

33. Wang X, Wang M, Xu Y, Yin J, Hu J. A 3D-printable gelatin/alginate/ε-poly-l-lysine hydrogel scaffold to enable porcine muscle stem cells expansion and differentiation for cultured meat development. *Int J Biol Macromol*. 2024; 271:131980. doi: 10.1016/j.ijbiomac.2024.131980

34. Yeong WY, Yu H, Lim KP, *et al*. Multiscale topological guidance for cell alignment via direct laser writing on biodegradable polymer. *Tissue Eng Part C Methods*. 2010;16(5):1011-1021. doi: 10.1089/ten.tec.2009.0604

35. Guven S, Chen P, Inci F, Tasoglu S, Erkmen B, Demirci U. Multiscale assembly for tissue engineering and regenerative medicine. *Trends Biotechnol*. 2015;33(5):269-279. doi: 10.1016/j.tibtech.2015.02.003

36. Kerativitayanan P, Carrow JK, Gaharwar AK. Nanomaterials for engineering stem cell responses. *Adv Healthc Mater*. 2015;4(11):1600-1627. doi: 10.1002/adhm.201500272

37. Rizzi R, Bearzi C, Mauretti A, Bernardini S, Cannata S, Gargioli C. Tissue engineering for skeletal muscle regeneration. *Muscles Ligaments Tendons J*. 2012;2(3):230-234.

38. Griffith LG, Swartz MA. Capturing complex 3D tissue physiology in vitro. *Nat Rev Mol Cell Biol*. 2006;7(3):211-224. doi: 10.1038/NRM1858

39. Dutta SD, Ganguly K, Jeong MS, *et al*. Bioengineered lab-grown meat-like constructs through 3D bioprinting of antioxidative protein hydrolysates. *ACS Appl Mater Interfaces*. 2022;14(30):34513-34526. doi: 10.1021/acsami.2c10620

40. Yi H, Forsythe S, He Y, *et al*. Tissue-specific extracellular matrix promotes myogenic differentiation of human muscle progenitor cells on gelatin and heparin conjugated alginate hydrogels. *Acta Biomater*. 2017;62:222-233. doi: 10.1016/j.actbio.2017.08.022

41. Rao KM, Kim HJ, Won S, Choi SM, Han SS. Effect of grape seed extract on gelatin-based edible 3D-hydrogels for cultured meat application. *Gels*. 2023;9(1):65.

doi: 10.3390/gels9010065

42. Valliant EM, Romer F, Wang D, *et al*. Bioactivity in silica/poly(γ-glutamic acid) sol–gel hybrids through calcium chelation. *Acta Biomater*. 2013;9(8):7662-7671. doi: 10.1016/j.actbio.2013.04.037

43. Li X, Wang X, Yao D, *et al*. Effects of aligned and random fibers with different diameter on cell behaviors. *Colloids Surf B Biointerfaces*. 2018;171:461-467. doi: 10.1016/j.colsurfb.2018.07.045

44. Tian F, Hosseinkhani H, Hosseinkhani M, *et al*. Quantitative analysis of cell adhesion on aligned micro- and nanofibers. *J Biomed Mater Res A*. 2008;84(2):291-299. doi: 10.1002/jbm.a.31304

45. Martino F, Perestrelo AR, Vinarský V, Pagliari S, Forte G. Cellular mechanotransduction: From tension to function. *Front Physiol*. 2018;9. doi: 10.3389/fphys.2018.00824

46. Davidenko N, Schuster CF, Bax D V., *et al*. Evaluation of cell binding to collagen and gelatin: A study of the effect of 2D and 3D architecture and surface chemistry. *J Mater Sci Mater Med*. 2016;27(10):148. doi: 10.1007/s10856-016-5763-9

47. Abdin M, Salama MA, Riaz A, Akhtar HMS, Elsanat SY. Enhanced the entrapment and controlled release of syzygium cumini seeds polyphenols by modifying the surface and internal organization of alginate-based microcapsules. *J Food Process Preserv*. 2021;45(1). doi: 10.1111/jfpp.15100

48. Levato R, Jungst T, Scheuring RG, Blunk T, Groll J, Malda J. From shape to function: The next step in bioprinting. *Adv Mater*. 2020;32(12). doi: 10.1002/adma.201906423

49. Tirella A, Orsini A, Vozzi G, Ahluwalia A. A phase diagram for microfabrication of geometrically controlled hydrogel scaffolds. *Biofabrication*. 2009;1(4):045002. doi: 10.1088/1758-5082/1/4/045002

50. Nam SY, Park SH. ECM based bioink for tissue mimetic 3d bioprinting. *Adv Exp Med Biol.* 2018; 1064:335-353. doi: 10.1007/978-981-13-0445-3_20

51. Malda J, Visser J, Melchels FP, *et al*. 25th anniversary article: Engineering hydrogels for biofabrication. *Adv Mater*. 2013;25(36):5011-5028. doi: 10.1002/adma.201302042

52. Sakai S, Yoshii A, Sakurai S, Horii K, Nagasuna O. Silk fibroin nanofibers: A promising ink additive for extrusion three-dimensional bioprinting. *Mater Today Bio*. 2020;8:100078. doi: 10.1016/j.mtbio.2020.100078

53. Jessop ZM, Al-Sabah A, Gao N, *et al*. Printability of pulp derived crystal, fibril and blend nanocellulose-alginate bioinks for extrusion 3D bioprinting. *Biofabrication*. 2019;11(4):045006. doi: 10.1088/1758-5090/ab0631

54. Markstedt K, Mantas A, Tournier I, Martínez Ávila H, Hägg D, Gatenholm P. 3D bioprinting human chondrocytes with nanocellulose–alginate bioink for cartilage tissue engineering applications. *Biomacromolecules*. 2015;16(5):1489-1496. doi: 10.1021/acs.biomac.5b00188

55. Seiti M, Mazzoldi EL, Pandini S, *et al*. FRESH 3D bioprinting of alginate – cellulose – gelatin constructs for soft tissue biofabrication. *Procedia CIRP*. 2024;125:42-47. doi: 10.1016/j.procir.2024.08.008

56. Distler T, McDonald K, Heid S, Karakaya E, Detsch R, Boccaccini AR. Ionically and enzymatically dual cross-linked oxidized alginate gelatin hydrogels with tunable stiffness and degradation behavior for tissue engineering. *ACS Biomater Sci Eng*. 2020;6(7):3899-3914. doi: 10.1021/acsbiomaterials.0c00677

57. Sonaye SY, Ertugral EG, Kothapalli CR, Sikder P. Extrusion 3D (bio)printing of alginate-gelatin-based composite scaffolds for skeletal muscle tissue engineering. *Materials*. 2022;15(22):7945. doi: 10.3390/ma15227945

58. Sonnleitner D, Schrüfer S, Berglund L, Schubert DW, Lang G. Correlating rheology and printing performance of fiber-reinforced bioinks to assess predictive modelling for biofabrication. *J Mater Res*. 2021;36(19):3821-3832. doi: 10.1557/s43578-021-00276-5

59. Hausmann MK, Rühs PA, Siqueira G, *et al*. Dynamics of cellulose nanocrystal alignment during 3D printing. *ACS Nano*. 2018;12(7):6926-6937. doi: 10.1021/acsnano.8b02366

60. Chaturvedi V, Dye DE, Kinnear BF, van Kuppevelt TH, Grounds MD, Coombe DR. Interactions between skeletal muscle myoblasts and their extracellular matrix revealed by a serum free culture system. *PLoS One*. 2015;10(6):e0127675. doi: 10.1371/journal.pone.0127675

61. Denes LT, Riley LA, Mijares JR, *et al*. Culturing C2C12 myotubes on micromolded gelatin hydrogels accelerates myotube maturation. *Skelet Muscle*. 2019;9(1):17. doi: 10.1186/s13395-019-0203-4

62. Jensen JH, Cakal SD, Li J, *et al*. Large-scale spontaneous self-organization and maturation of skeletal muscle tissues on ultra-compliant gelatin hydrogel substrates. *Sci Rep*. 2020;10(1):13305. doi: 10.1038/s41598-020-69936-6

63. Spedicati M, Zoso A, Mortati L, Chiono V, Marcello E, Carmagnola I. Three-dimensional microfibrous scaffold with aligned topography produced via a combination of melt-extrusion additive manufacturing and porogen leaching for in vitro skeletal muscle modeling. *Bioengineering*. 2024;11(4):332. doi: 10.3390/bioengineering11040332

64. Engler AJ, Sen S, Sweeney HL, Discher DE. Matrix elasticity directs stem cell lineage specification. *Cell*. 2006;126(4):677-689.

doi: 10.1016/j.cell.2006.06.044

65. Cui W, Huang Y, Chen L, *et al*. Tiny yet tough: Maximizing the toughness of fiber-reinforced soft composites in the absence of a fiber-fracture mechanism. *Matter*. 2021;4(11):3646-3661.
doi: 10.1016/j.matt.2021.08.013

66. Heher P, Maleiner B, Prüller J, *et al*. A novel bioreactor for the generation of highly aligned 3D skeletal muscle-like constructs through orientation of fibrin via application of static strain. *Acta Biomater*. 2015;24:251-265.
doi: 10.1016/j.actbio.2015.06.033

67. Schwab A, Levato R, D'Este M, Piluso S, Eglin D, Malda J. Printability and shape fidelity of bioinks in 3D bioprinting. *Chem Rev Am Chem Soc*. 2020;120(19):11028-11055.
doi: 10.1021/acs.chemrev.0c00084

68. Heck T, Faccio G, Richter M, Thöny-Meyer L. Enzyme-catalyzed protein crosslinking. *Appl Microbiol Biotechnol*. 2013;97(2):461-475.
doi: 10.1007/s00253-012-4569-z

69. Kashiwagi T, Yokoyama K ichi, Ishikawa K, *et al*. Crystal Structure Of Microbial Transglutaminase From Streptoverticillium mobaraense. *J Biol Chem*. 2002;277(46):44252-44260.
doi: 10.1074/jbc.M203933200

70. Kitzmann M, Carnac G, Vandromme M, Primig M, Lamb NJC, Fernandez A. The muscle regulatory factors MyoD and Myf-5 undergo distinct cell cycle–specific expression in muscle cells. *J Cell Biol*. 1998;142(6):1447-1459.
doi: 10.1083/jcb.142.6.1447

71. Yang HS, Lee B, Tsui JH, *et al*. Electroconductive nanopatterned substrates for enhanced myogenic differentiation and maturation. *Adv Healthc Mater*. 2016;5(1):137-145.
doi: 10.1002/adhm.201500003

72. Niknezhad SV, Mehrali M, Khorasgani FR, *et al*. Enhancing volumetric muscle loss (VML) recovery in a rat model using super durable hydrogels derived from bacteria. *Bioact Mater*. 2024;38:540-558.
doi: 10.1016/j.bioactmat.2024.04.006

73. Kim K, Jin S, Shin M. Effect of 3D-printable anisotropic fibrous hydrogels on fabricating artificial skeletal muscle constructs. *Adv Ther (Weinh)*. 2024;7(1).
doi: 10.1002/adtp.202300170

74. Lee S, Kim W, Kim G. Efficient myogenic activities achieved through blade-casting-assisted bioprinting of aligned myoblasts laden in collagen bioink. *Biomacromolecules*. 2023;24(11):5219-5229.
doi: 10.1021/acs.biomac.3c00749

75. Li Q, Yu S, Wang Y, *et al*. Programmable embedded bioprinting for one-step manufacturing of arterial models with customized contractile and metabolic functions. *Trends Biotechnol*. 2025;43(4):918-945.
doi: 10.1016/j.tibtech.2024.11.019